Extracellular Matrix Viscoelasticity Drives Liver Cancer Progression in Pre-Cirrhotic NASH

Natalie Török (ntorok@stanford.edu)
Stanford
Weiguo Fan
Stanford
Kolade Adebowale
Stanford
Yuan Li
Stanford
Md Foysal Rabbi
Purdue University https://orcid.org/0000-0003-3214-2209
Lorand Vancza
Stanford
Dongning Chen
Stanford
Koshi Kunimoto
Stanford
Gergely Mozes
Stanford
Yisi Li
Tsinghua University
Junyan Tao
Unviersity of California, San Francisco
Satdarshan Monga
University Of Pittsburgh https://orcid.org/0000-0002-8437-3378
Gregory Charville
Stanford University School of Medicine https://orcid.org/0000-0002-2774-2704
Rebecca Wells
University of Pennsylvania https://orcid.org/0000-0002-6988-4102
Renu Dhanasekaran
Stanford University
Taeyoon Kim
Purdue University
Ovijit Chaudhuri

Stanford University https://orcid.org/0000-0002-9287-3401

Biological Sciences - Article

Keywords:

Posted Date: October 10th, 2022

DOI: https://doi.org/10.21203/rs.3.rs-2087090/v1

Extracellular Matrix Viscoelasticity Drives Liver Cancer Progression in Pre-Cirrhotic NASH

Authors:

Weiguo Fan[1], Kolade Adebowale[2,3], Yuan Li[1], Md Foysal Rabbi[4], Lorand Vancza[1], Dongning Chen[1], Koshi Kunimoto[1], Gergely Mozes[1], Yisi Li[5], Junyan Tao[6], Satdarshan P. Monga[6], Gregory W. Charville[7], Rebecca G. Wells[8], Renumathy Dhanasekaran[1], Tae Yoon Kim[4], Ovijit Chaudhuri[3,9] and Natalie J. Török[1*]

Affiliations:

1. Gastroenterology and Hepatology, Stanford University, 300 Pasteur Dr, and VA Palo Alto, CA 94304, USA

2. Department of Chemical Engineering, Stanford University, Stanford, CA, USA

3. Chemistry, Engineering, and Medicine for Human Health (ChEM-H), Stanford University, Stanford, CA, USA

4. Weldon School of Biomedical Engineering, Purdue University, West Lafayette, Indiana, United States of America

5. Department of Automation, Tsinghua University, Beijing 100084, China.

6. Department of Pathology and Pittsburgh Liver Research Center, University of Pittsburgh and University of Pittsburgh Medical Center, Pittsburgh PA, USA.

7. Department of Pathology, Stanford University, 300 Pasteur Dr, Stanford, CA 94304.

8. Department of Medicine, University of Pennsylvania, Philadelphia, PA, USA.

9. Department of Mechanical Engineering, Stanford University, Stanford, CA, USA.

*Corresponding author: Natalie J. Török, MD. MSc. Division of Gastroenterology and Hepatology, Stanford School of Medicine, 300 Pasteur Dr., Alway Building Room M207, Stanford CA 94305, and Palo Alto VA, 3801 Miranda Dr, Palo Alto, CA 94304. Email: ntorok@stanford.edu. Phone: (650) 723-2188.

The authors have declared that no conflict of interest exists.

Abstract:

Type 2 diabetes mellitus (T2DM) is a major risk factor for hepatocellular carcinoma (HCC). Changes in extracellular matrix (ECM) mechanics contribute to cancer development[1,2], and increased stiffness is known to promote HCC progression in cirrhotic conditions[3,4]. T2DM is characterized by an accumulation of advanced glycation end products (AGEs) in the ECM; however, how this affects HCC in non-cirrhotic conditions is unclear. Here, we find that in patients and animal models AGEs promote changes in collagen architecture and enhance ECM viscoelasticity, with greater viscous dissipation and faster stress relaxation, but not changes in stiffness. High AGEs and viscoelasticity combined with oncogenic β-catenin signaling promote HCC induction, while inhibiting AGEs production, reconstituting the clearance receptor AGER1, or breaking AGE-mediated collagen crosslinks reduce viscoelasticity and HCC growth. Matrix analysis and computational modeling demonstrate that lower interconnectivity of AGEs-bundled collagen matrix, marked by shorter fiber length and greater heterogeneity, enhance viscoelasticity. Mechanistically, animal studies and 3D cell cultures show that enhanced viscoelasticity promotes HCC cell proliferation and invasion through integrin β1–Tensin 1–YAP mechanotransduction pathway. These results reveal for the first time that AGEs-mediated structural changes enhance ECM viscoelasticity, and that viscoelasticity can drive cancer progression in vivo, independent of stiffness.

Main

T2DM and obesity are important risks for HCC, and it is estimated that up to 30% of HCCs in nonalcoholic steatohepatitis (NASH) occur at a pre-cirrhotic stage when matrix stiffness is still low, and these patients often have poor glycemic control[5,6]. Interestingly, ECM changes can be driven by the accumulation of AGEs in this population. AGEs are produced by the non-enzymatic glycation of serum or tissue proteins during T2DM or can be ingested orally through the consumption of food prepared at high temperatures[7]. Over time AGEs accumulate in the matrix due to decreased clearance and metabolism[8-10], and can biochemically modify collagen and ECM proteins[11]. While AGEs in NASH do not appear to increase stiffness greatly, they could impact ECM viscoelasticity. Tissues and ECMs are generally viscoelastic, exhibiting viscous energy dissipation in response to mechanical perturbations and a time-dependent mechanical response, such as stress relaxation in response to deformation[12]. Recent work has shown that changes in

ECM viscoelasticity, independent of stiffness, have impacted cell behaviors, including proliferation and migration of breast cancer cells[13-16]. Here we investigated the role of AGE-mediated changes in ECM mechanical properties on NASH and HCC progression.

Accumulation of AGEs enhances liver viscoelasticity

To evaluate the potential role of AGE-mediated changes in ECM properties in NASH, we studied the mechanical properties of liver samples from patients with NASH with or without T2DM (average nonalcoholic fatty liver disease activity [NAS] score 4, fibrosis stage 0-1) (Fig. 1a). Liver AGEs were significantly higher in patients with NASH/T2DM compared to those without T2DM (Fig. 1b). Using atomic force microscopy (AFM), we found that patients with T2DM had similar stiffness (Fig. 1c, d) but higher hysteresis area under loading-unloading cycles, corresponding to viscous energy dissipation or loss, and indicating higher viscoelasticity (Fig. 1e, f). Furthermore, using rheometry, we confirmed that livers of non-cirrhotic NASH/T2DM patients had similar storage moduli but a higher loss tangent and faster stress relaxation under a constant deformation (Fig. 1g-k).

To investigate the potential link between AGEs accumulation and enhanced viscoelasticity, we studied a NASH mouse model on a high AGEs diet (HiAD)[10]. HiAD-fed mice exhibit steatosis, hepatocyte ballooning, insulin resistance, and higher liver AGEs compared to those on regular (chow) or fast-food diets (FFD) (Fig. 1l, m). Mice on HiAD had similar stiffness (Fig. 1n, q), but increased viscoelasticity (Fig. 1o, p and r-t), compared to those fed chow or FFD, as assessed by AFM or rheometry, respectively. Significantly, inhibiting AGEs production with Pyridoxamine (PM) or preventing the formation of AGEs-collagen crosslinks with alagebrium (ALT) could reverse the changes in viscoelasticity (Fig. 1o, p and r-t). Together, these data indicate that AGEs-mediated changes in the ECM cause enhanced liver viscoelasticity.

AGEs-enhanced viscoelasticity generates a tumorigenic niche for HCC

The above results prompted us to investigate the potential causal connections between ECM viscoelasticity and HCC progression. Previous studies on NASH-related HCC commonly used high-fat diet combined with the carcinogen diethylnitrosamine (DEN), genetically modified models, or long-term feeding e.g., CDAA diet[17]. However, DEN-induced HCCs depend on genotoxic signals and lack the typical pathogenesis in patients characterized by cell injury and

inflammation preceding HCC[18]. To experimentally imitate the conditions with increasing ECM stress relaxation prior to HCC onset, we used a more pathophysiologically relevant model to modulate the metabolic/matrix milieu prior to tumor seeding. We hydrodynamically delivered human hMet with mutant-β-catenin[19] or control vectors to chow, FFD or HiAD-fed mice. Earlier appearance and faster growth of transformed foci (GS and myc-tag positive) were observed in HiAD-fed mice compared to those on chow or FFD diet (Fig. 2a-c, and Extended Data 1a-c). Importantly, HCC growth was diminished and survival rate improved after AGEs inhibition with PM or breaking collagen/AGEs crosslinks with ALT (Fig. 2d-g, and Extended Data 1d-f).

We next modulated AGEs receptor activity using two additional approaches. First, we addressed AGER1 (AGEs clearance receptor). As patients with T2DM/NASH and mice on HiAD have significantly downregulated AGER1[10], we sought to reverse this with an AAV8- mediated AGER1 delivery prior to the hydrodynamic injection (HDI) (Fig. 2h). These mice had lower AGEs (Fig. 2i) due to improved uptake, similar stiffness (Fig. 2j) but lower stress relaxation (Fig. 2 k, l, Extended Data 1h), and reduced growth of tumor foci, compared to mice injected with the control AAV8 construct (Fig. 2m, n, and Extended Data 1g).

Second, we studied HCC in mice with RAGE (proinflammatory AGEs receptor) hepatocyte deletion ($RAGE^{HepKO}$), and hydrodynamically injected human hMet with mutant-β-catenin (Extended Data Fig. 2a). These mice had reduced growth of tumor foci, compared to mice with *fl/fl* RAGE background on HiAD (Extended Fig. 2a-c), decreased liver AGEs (Extended Fig. 2d), similar stiffness (Extended Fig. 2e), and reduced stress relaxation (Extended Data Fig. 2f-h).

Together, these studies with four animal models all converge on the conclusion that AGEs accumulation in the ECM creates a more viscoelastic and tumorigenic environment that promotes HCC progression.

AGEs modulate collagen network architecture and connectivity leading to enhanced viscoelasticity

The data presented so far suggest that AGEs accumulation in the liver is critical to enhanced ECM viscoelasticity and HCC progression, so we next sought to elucidate how AGEs accumulation modulates ECM viscoelasticity. Type-1 collagen networks are thought to be critical regulators of tissue mechanics[20]. AGEs can directly crosslink collagen and affect matrix mechanics by altering

its helical structure[21,22]. Inhibiting AGEs production or disrupting AGEs/collagen crosslinks in the HiAD model decreased the amount of highly crosslinked insoluble collagen (Fig. 3a). Two-photon imaging and second harmonic generation microscopy techniques were employed to analyze the decellularized native ECM from chow or HiAD-fed mice to evaluate collagen architecture, specifically fiber length, spatial orientation, and interconnectivity. Compared to the well-organized collagen network in mice on chow diet, in HiAD-fed mice the network exhibited less connectivity with crosslinked collagen bundles that had shorter fibers and displaying greater heterogeneity (Fig. 3b). Similar structures were seen in neutralized reconstituted collagen hydrogels exposed to AGEs (Fig. 3c). Next, rheological measurements were done to evaluate the viscoelastic properties of AGEs-crosslinked collagen hydrogels to study the relationship between low connectivity collagen networks and matrix characteristics. AGEs-crosslinked collagen hydrogels showed similar stiffness (Fig. 3d) but faster stress relaxation than non-crosslinked collagen (Fig. 3e). To confirm these results in a collagen-rich matrix with stiffness comparable to that of the liver, interpenetrating polymer network (IPN) 3D hydrogels made by AGEs-modified collagen and alginate were tested (Fig. 3f). Similar changes in collagen architecture and connectivity were found in collagen IPN gels (Fig. 3g). Breaking the AGEs-collagen crosslinks with ALT decreased the amount of insoluble collagen (Fig. 3h) and improved fiber length, fiber-fiber angle, and network connectivity (Fig. 3i, j). Furthermore, indentation test showed improved viscoelasticity after AGE-collagen crosslink breaking by ALT (Fig. 3k). IPN hydrogels mixed with AGEs-modified collagen also showed similar stiffness (Fig. 3l) but faster stress relaxation compared to non-modified collagen (Fig. 3m-o) based on rheological measurements.

To further study how matrix architecture impacts viscoelasticity, we simulated collagen matrices with a variation in two structural parameters to model the activity of AGEs: average collagen fiber bundle length and bundling angle, as a proxy for heterogeneity (Fig. 3p, q). The collagen matrices are connected by a combination of weak bonds, known to act within and between collagen fibers and underlie stress relaxation and viscoelasticity in type-1 collagen matrices, and covalent crosslinks due to AGEs activity (Extended Data Fig. 3 and Extended Data Fig. 4)[23-25]. Bundled networks are more heterogeneous, and exhibit faster stress relaxation than unbundled networks (Fig. 3r). Reducing fiber length (Fig. 3s and Extended Data Fig. 5) or reducing the bundle angle (Fig. 3t and Extended Data Fig. 6), increases the heterogeneity of the network and leads to faster stress relaxation. Together, these computational results show that the changes in architecture that

are observed due to AGEs activity in vivo and in vitro, namely enhanced heterogeneity and shorter fiber length, are predicted to lead to faster stress relaxation and enhanced viscoelasticity.

ECM viscoelasticity promotes YAP activation through tensin-1 (TNS1), mediated by integrin-β1-dependent mechanotransduction

Next, we focused on the mechanotransductive pathways that could lead to tumor growth and invasion by faster stress relaxation. RNA sequencing and bioinformatics analyses were performed on mouse liver samples (chow, FFD, HiAD, HiAD plus PM, and $RAGE^{HepKO}$), to identify potential mechanosensitive pathways. Kyoto Encyclopedia of Genes and Genomes (KEGG) analyses were performed on differentially expressed genes between HiAD and FFD to categorize the enriched functional classification. In the Hippo signaling pathway group, YAP/TAZ regulated genes were enriched in HiAD-fed mice, and decreased after PM treatment and in $RAGE^{hepKO}$ (Fig. 4a-c). In the mouse models, we saw YAP activation and nuclear translocation in HiAD mice but significantly less after PM or in the $RAGE^{hepKO}$ (Fig. 4d, e). To substantiate that HCC progression in faster stress-relaxing ECM was driven by YAP/TAZ, we co-injected dominant-negative (dn) TEAD2 plasmid with mutant β-catenin during HDI (Fig. 4f). We found that the number of GS/myc double positive foci significantly decreased after (dn) TEAD2 co-injection compared to those injected with the control plasmid (Fig. 4g, h).

Given these results, our next question was how faster stress relaxing ECM conveys proliferative and/or invasive signals to promote HCC progression. First, to directly test the effects of matrix viscoelasticity, we constructed IPNs of alginate and reconstituted basement membrane (rBM) matrix hydrogels for 3D culture studies (rBM-IPNs). HCC cells (Huh7) were encapsulated in rBM-IPN hydrogels[16,26] with the same stiffness (Young's modulus 2kPa to mimic the human liver) but different levels of viscoelasticity (Fig. 5a). After 24 hours in culture, cells exhibited YAP activation (Fig. 5b, e), enrichment in cortactin with invadopodia formation and shape changes (Fig. 5c, f), as well as proliferation (Fig. 5d, g) in high viscoelasticity gels. As β1-integrin–matrix interactions modulating mechanotransduction were reported in breast cancer cells in high viscoelasticity gels[16,26], we used integrin β1-specific blocking antibodies, and this reduced YAP activation (Fig. 5h), cell circularity (Fig. 5i and Extended Data Fig. 7a), and proliferation (Fig. 5j).

Pharmacological inhibition of the downstream signaling elements, ROCK-GTPase and myosin 2 resulted in similar findings (Fig. 5k-m and Extended Data Fig. 7b).

Interestingly, based on our RNAseq data, we found that Tensin 1 (TNS1) was significantly induced in an AGEs and viscoelasticity-dependent manner (Fig. 4c and Fig. 5n). TNS1 was described as part of a molecular clutch that mediates the mechanical linkage between ECM-bound integrins and the acto-myosin cytoskeleton and linked to traction force generation[27-31]. To study the role of TNS1 in mechano-signaling, first, proximity ligation assays (PLA) were performed on Huh7 cells in high and low viscoelasticity hydrogels to capture the potential interaction of TNS1 with integrin β1. High viscoelasticity conditions promoted their interaction (Fig. 5o, p). TNS1 knockdown (KD) in Huh7 cells by Crisp/cas9 reduced activation of YAP and proliferation in fast relaxing hydrogels (Fig. 5q, r). These data suggest that TNS1 is part of a molecular clutch that mediates the mechanical linkage between ECM-bound integrins and the actomyosin cytoskeleton responding to high viscoelasticity (Fig. 5s).

Discussion

In this study we show that AGEs in the liver ECM create a faster stress-relaxing viscoelastic niche leading to the activation of mechano-signaling pathways promoting HCC progression. While matrix stiffness in advanced fibrosis/cirrhosis and its effects on cancer progression have extensively been studied, our data are the first demonstrating how changes in viscoelasticity of the microenvironment, independent of stiffness, impact HCC growth. This is clinically very relevant as increasing viscoelasticity could be a new risk factor foretelling more invasive features of HCC in NASH/T2DM. Current guidelines exclude pre-cirrhotic patients from HCC screening paradigms, therefore new viscoelasticity-based imaging approaches will need to be developed to identify the population at risk. T2DM is a major risk factor for not only liver cancer progression but also in breast[32], colon[33], and pancreatic cancer[34-36] and this may point to the crucial role of a more viscoelastic matrix in diabetic patients.

Collagen crosslinking mediated by AGEs has been thought to contribute to increasing stiffness similarly to e.g. LOXl2 or TTG, modifying the helical structure of collagen[37-39]. However, our studies unraveled that in certain contexts, increased collagen crosslinking leads to weakly bound collagen fibers with lower interconnectivity and shorter fibers, together promoting a viscoelastic niche. This in turn, facilitates cellular shape changes, cytoskeletal reorganization, and invadopodia

formation[12,13,15,16]. This could be relevant to not only the liver peritumoral matrix, but other cancers where changes in viscoelasticity are observed, but not yet implicated functionally for progression [40,41].

We also identified the major role of TNS1-integrin β1-YAP mechano-transduction pathway responding to increasing viscoelasticity. While the role of YAP activation in various cancers is known, as is its role in responding to viscoelasticity in vitro[14,15,26,42,43], the in vivo role of YAP activation as an inducer of cancer progression in response to changes in ECM viscoelasticity was previously unknown. Further, another element of interest relates to the role of TNS1 as a key mechanosensory in this integrin-YAP signaling pathway. TNS1 regulating and sustaining the activity of the molecular clutch could be essential for invadopodia formation and migratory activity of cells[27,28], and these can be further explored in future studies. Interestingly, TNS1 has clinically been linked to worse HCC outcomes in patients with non-viral and non-alcoholic HCC (Extended Data Fig. 7c). This raises the possibility that TNS1 can have a key role not only in early invasion but at later stages, with metastatic activity of tumor cells.

In conclusion, we uncovered the central role of increasing viscoelasticity in the liver tumor niche. Viscoelasticity-activated mechano-cellular pathways promise to be a novel diagnostic and/or therapeutic area in NASH/T2DM-related HCC and beyond.

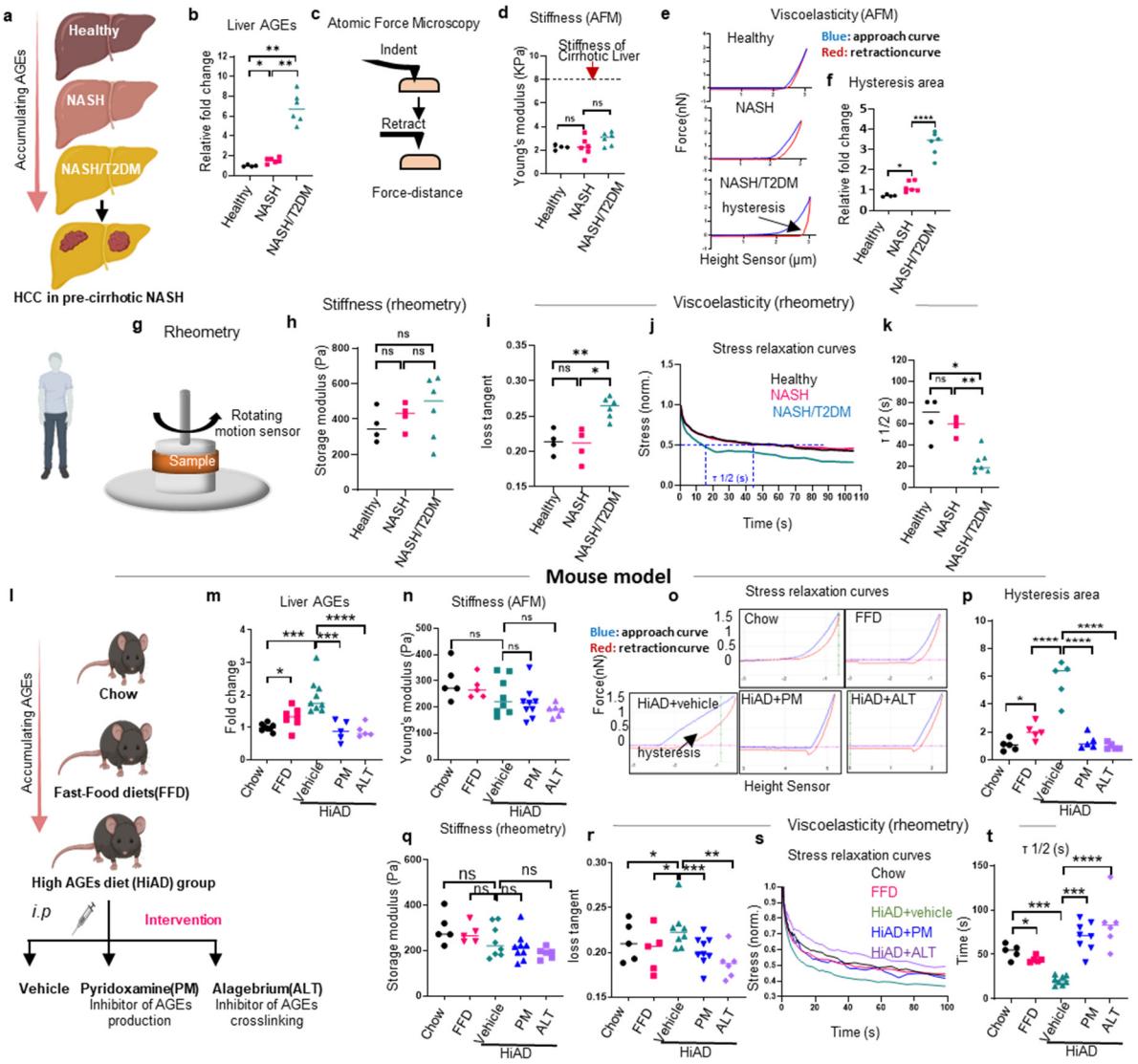

Fig. 1: Viscoelasticity is increased in livers of patients with NASH/T2DM and mice on a high AGEs diet.

a. Schematic representation of AGEs increase in NASH/T2DM. The illustration was created using BioRender.com.

b. AGEs are increased in livers of NASH/T2DM patients compared to healthy or NASH livers (n=4-6, mean±SEM, *P < 0.05, **P < 0.01, ANOVA).

c. Schematic of the Atomic Force Microscopy (AFM). Indent-retract was used to get force-distance curves. Indent-constant height was used to get stress relaxation curves.

d. Atomic Force Microscopy (AFM) experiments were performed on snap-frozen human liver samples from healthy subjects and those with NASH or NASH with T2DM, respectively. Liver stiffness is represented as Young's modulus. (n=4-6, mean±SEM, ns not significant, ANOVA, Tukey's post hoc). The average stiffness of a human cirrhotic liver was indicated by a dashed line.

e, f. Representative force-distance curves show larger hysteresis areas (arrow, the area between approach and retraction force curves) in patients with T2DM (**e**). Trapz function in MATLAB was used to measure the hysteresis area in (e), 50 force-distance curves were measured in each sample, each group (**f**). (n=4-6, mean±SEM, $*P < 0.05$, $****P < 0.0001$, ANOVA).

g. Schematics depicting the rheometry tests performed on human fresh liver tissues.

h, i. Rheometry was performed with 100~300 Pa of initial force. Dynamic time sweep test (2% constant strain, oscillation frequency 1 radian/s, measurements for 600s) was done first to collect the storage modulus (stiffness) and loss tangent. There were no significant differences between healthy samples and those from NASH w/o T2DM. Dynamic time sweep test showed a significant change of loss tangent (**i**) but not storage modulus (stiffness) (**h**) in livers from NASH patients with T2DM (n=4-6, mean±SEM, $*P < 0.05$, $**P < 0.01$, ns not significant, ANOVA).

j, k. Stress relaxation test was performed for 110s with an initial 10% strain, and quantification of timescales at which the stress is relaxed to half its original value ($\tau 1/2$). The representative stress relaxation curves demonstrated that samples from NASH/T2DM patients had faster stress relaxation (**j**). Stress was normalized to the initial stress (**k**). (n=4-6, mean±SEM, $*P < 0.05$, $**P < 0.01$, ns not significant, ANOVA).

l, Mice were placed on Chow, fast food diet (FFD) or high AGEs diet (HiAD) for 14 weeks. On HiAD diet, a group of mice either received a daily vehicle (Tris-HCl), or AGEs inhibitor (Pyridoxamine, PM, 60 mg/kg), or AGEs crosslinking inhibitor (Alagebrium, ALT, 1mg/kg).

m, Liver AGEs increased in mice on HiAD and decreased following PM or ALT treatment. (n=5-9, mean±SEM, $*P < 0.05$, $***P < 0.001$, $****P < 0.0001$, ANOVA).

n-p, AFM was performed on the liver samples. Liver stiffness was not significantly different between the groups (**n**). Force-distance curves in livers from HiAD-fed mice exhibit larger hysteresis areas (arrow) than those on chow or FFD. The hysteresis was reduced in PM or in ALT-

259 treated mice (**o**). Trapz function in MATLAB was used to measure the hysteresis area in (o), (**p**).
260 (n=5-9, mean±SEM, *P < 0.05, ****P < 0.0001, ns not significant, ANOVA).
261 **q-t**, Rheometry data show that stiffness in HiAD-fed mice was comparable to chow, FFD-fed mice
262 or those treated with PM or ALT (**q**). HiAD however, induced a higher loss tangent (**r**) and faster
263 stress relaxation, which improved by PM or ALT-711 treatment (**s, t**). (N=5-8, mean ± SEM;
264 *p<0.05, **p<0.01, ***p<0.001, ****p<0.0001, ns not significant, ANOVA, post-hoc Tukey test).

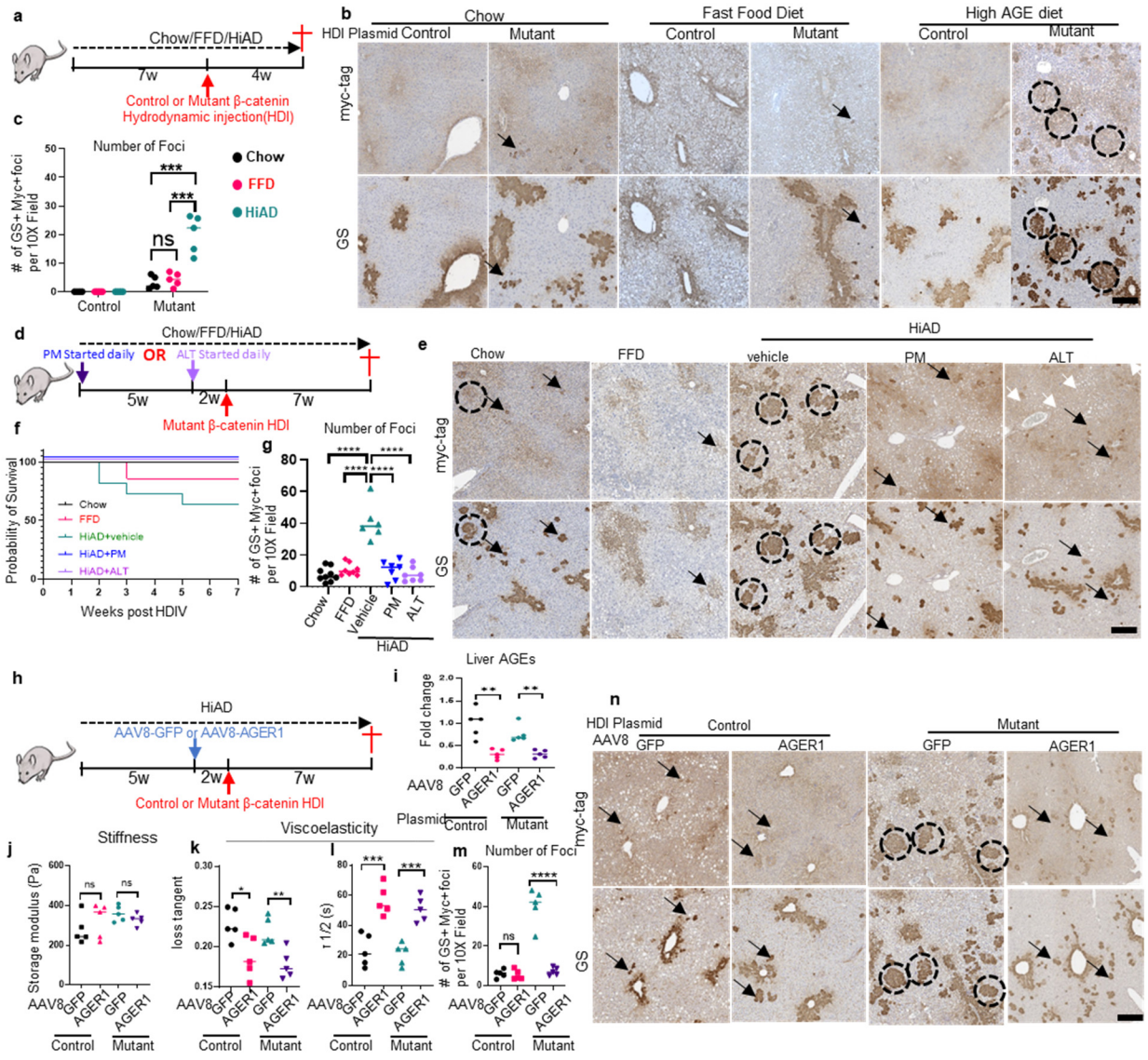

Fig. 2: Mice on HiAD develop more tumor foci following hydrodynamic injection, and exhibit AGEs-dependent higher viscoelasticity.

a. Schematics of the NASH-related hepatocellular carcinoma (HCC) models. Mice were fed for 7 weeks either chow, FFD or HiAD. Hydrodynamic injection (HDI) was performed using vectors expressing human MET gene (pT3-EF5a-hMet-V5), and sleeping beauty (SB) transposase combined with a vector expressing either wild-type human β-catenin (pT3-EF5a-β-catenin-myc, control group) or mutant pT3-EF5a-S45Y-β-catenin -myc, mutant group). Four weeks after HDI, mice were sacrificed for analysis.

b. Immunohistochemistry, co-localization of glutamate synthetase (GS) and myc-tag positive foci (more than 20 cells are considered forming a focus (circles). Scattered cells denote transduced cells (arrows). GS at baseline marks pericentral cells. Scale bar, 300 μm.

c. Quantification of GS and myc positive foci. (N=5, mean ± SEM; ***p<0.001, ns not significant, ANOVA, post-hoc Tukey test)

d. Schematics of the NASH-related HCC model combined with AGEs lowering interventions. Mice were fed for 7 weeks either chow, FFD or HiAD. On the HiAD diet, groups of mice either received daily vehicle, or PM (started at the time of the diet), or ALT (started after 5 weeks of diet). HDI was performed using hMet and mutant β-catenin, with the SB transposase.

e. GS/myc immunohistochemistry in mice on chow, FFD and HiAD following HDI and PM/ALT, vs. vehicle treatment.

f. Survival rates of mice after HDI. The worst survival at 7 weeks post-HDI was for HiAD-fed mice (+vehicle); this improved in PM-or ALT-treated mice.

g. Quantification of tumor foci **7** weeks post-HDI. PM and ALT treatment lowered the number of GS/myc tag positive foci Scale bar, 300 μm. (N=6-8, mean ± SEM; ****P < 0.0001, ANOVA, post-hoc Tukey test).

h. Schematic presentation of the NASH-related HCC model combined with AAV8-mediated AGER1 induction prior to HDI. Mice were fed HiAD and AGER1 was reconstituted by injecting AAV8-TBG-AGER1 2w prior to the HDI. As control AAV8-TBG-GFP was used. HDI was performed using hMet/SB transposase with wild-type (control) or mutant β-catenin.

i. Liver AGEs in mice were reduced by AGER1 delivery. (n=5, mean±SEM, ***P < 0.001, ANOVA).

j-l. Rheometry data showing no significant difference in stiffness (**j**) but improved viscoelasticity (**k** and **l**) in AGER1 reconstituted mice. (N=5, mean ± SEM; *p<0.05, **p<0.01, ***p<0.001, ns not significant, ANOVA, post-hoc Tukey test).

m, n. Quantification of foci (**m**) and GS/myc by immunohistochemistry (**n**). Scale bar, 300 μm. (N=5, mean ± SEM; ****P < 0.0001, ns not significant, ANOVA, post-hoc Tukey test).

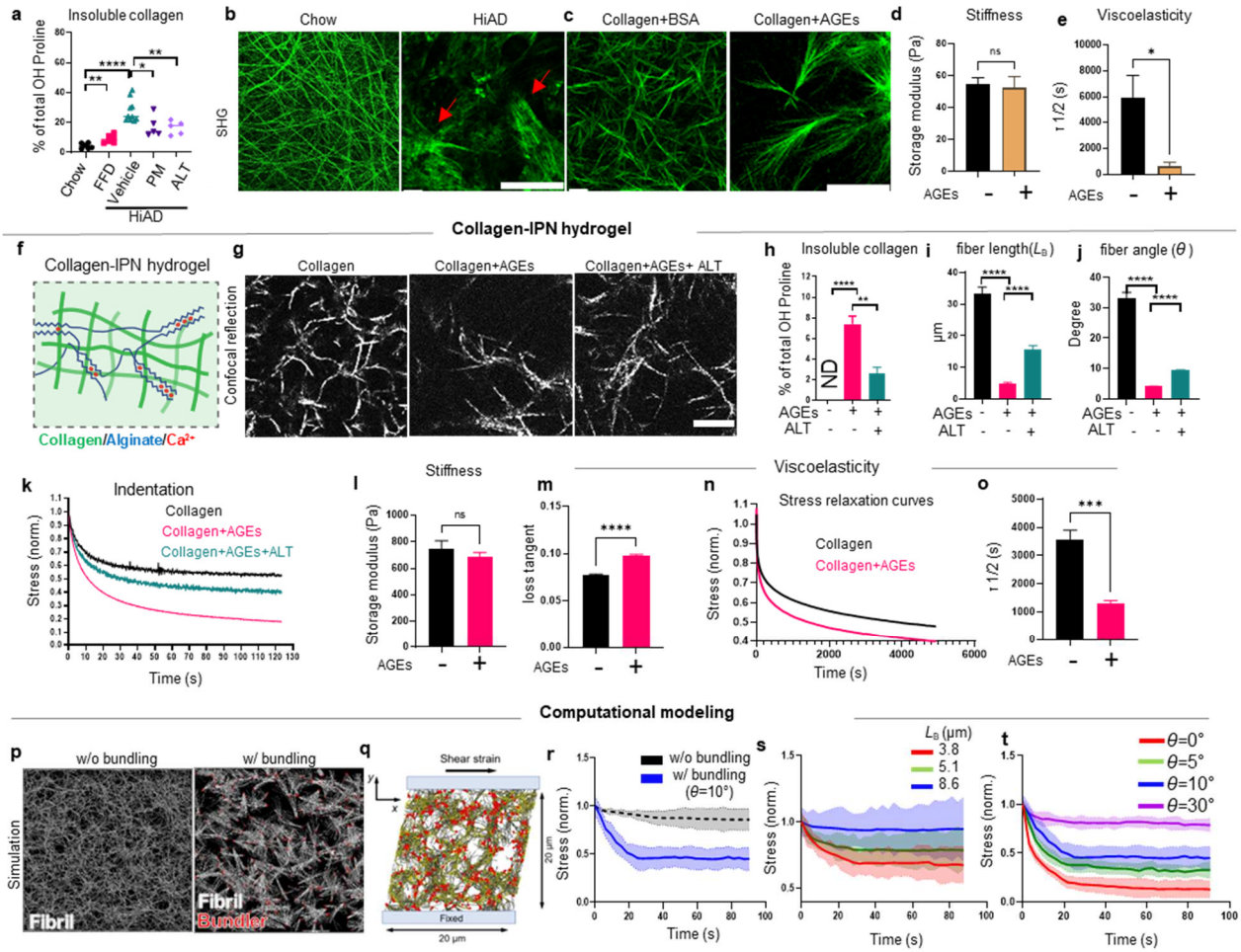

Fig. 3 AGEs modulate collagen architecture and network connectivity leading to enhanced viscoelasticity in mouse livers and 3D hydrogels.

a. Quantification of insoluble collagen on different diets. Collagen insolubility improved after PM or ALT in mic on HiAD. (N=5-10, mean ± SEM; *p<0.05, **p<0.01, ***p<0.001, ****P < 0.0001, ANOVA, post-hoc Tukey test).

b. Collagen fibers in decellularized liver ECM from chow and HiAD-fed mice were analyzed by second harmonic generation (SHG) microscopy. Red arrows indicate altered collagen architecture with bundle formation. Scale bar, 100 μm.

c. Collagen fibers in collagen hydrogels were analyzed by SHG. Collagen was pre- incubated with BSA or AGEs at 4 ℃ for 4 weeks. AGEs promoted bundling of fibers, scale bar, 100 μm.

d, e. Collagen hydrogels from **(c)** were loaded on the rheometer for stiffness (**d**, storage modulus) and viscoelasticity testing expressed as T1/2 (**e**). (n=4-5, mean ± SEM, ***p<0.001, ****P < 0.0001, ns not significant, one-way ANOVA, post-hoc Tukey test).

f. Schematics of the collagen/interpenetrating polymer network (IPN) hydrogel based on a physical network of collagen and calcium alginate (Alg-Ca^{2+}). IPN gels were generated by collagen w/wo AGEs modified and Alg-Ca^{2+} (same concentration between gels).

g. Confocal reflectance microscopy shows altered collagen fibers following addition of AGEs . Collagen was incubated with AGEs+/- ALT cross-link inhibitor, then mixed with high molecular weight alginate to generate interpenetrating polymer network (IPN) hydrogels. scale bar, 100 μm.

h. Quantification of insoluble collagen in the IPN hydrogels, following AGEs+/- ALT-711 treatment.

i, j. Quantification of collagen fiber length (**i**) (CT-Fire software) and angle (**j**) (image J) in IPN gels. 10 pictures were measured in each sample, in each group (n=5, mean ± SEM; ****P < 0.0001, ANOVA, post-hoc Tukey test).

k. Representative stress relaxation curves from IPN gels were tested by Instron 5848, 10 N load.

l-o. IPN gels were loaded on the rheometer for stiffness (**l**, storage modulus) and viscoelasticity testing (**m-o**). Viscoelasticity is represented by loss tangent (**m**) and stress relaxation (**n, o**). (N=5, mean ± SEM, ***p<0.001, ****P < 0.0001, ns not significant, one-way ANOVA, post-hoc Tukey test).

p. Simulation modeling. A matrix structure consisting of individual fibrils without any bundler (left) or connecting the ends of fibrils with a specific angle (θ = 10°) (right). In both matrix structures, the length of all fibrils is 3 μm.

q. After a matrix is assembled in a rectangular computational domain (20×20×5 μm), the matrix is rapidly deformed by shear strain linearly increasing up to 20%. Gray, yellow, and red indicate fibrils, cross-linkers, and bundlers, respectively.

r. Stress relaxation is measured using the two matrices shown in **p**.

s, t. Stress relaxation is measured using matrices with different bundle length (LB) (**a**) or different bundling angle (θ)(**t**).

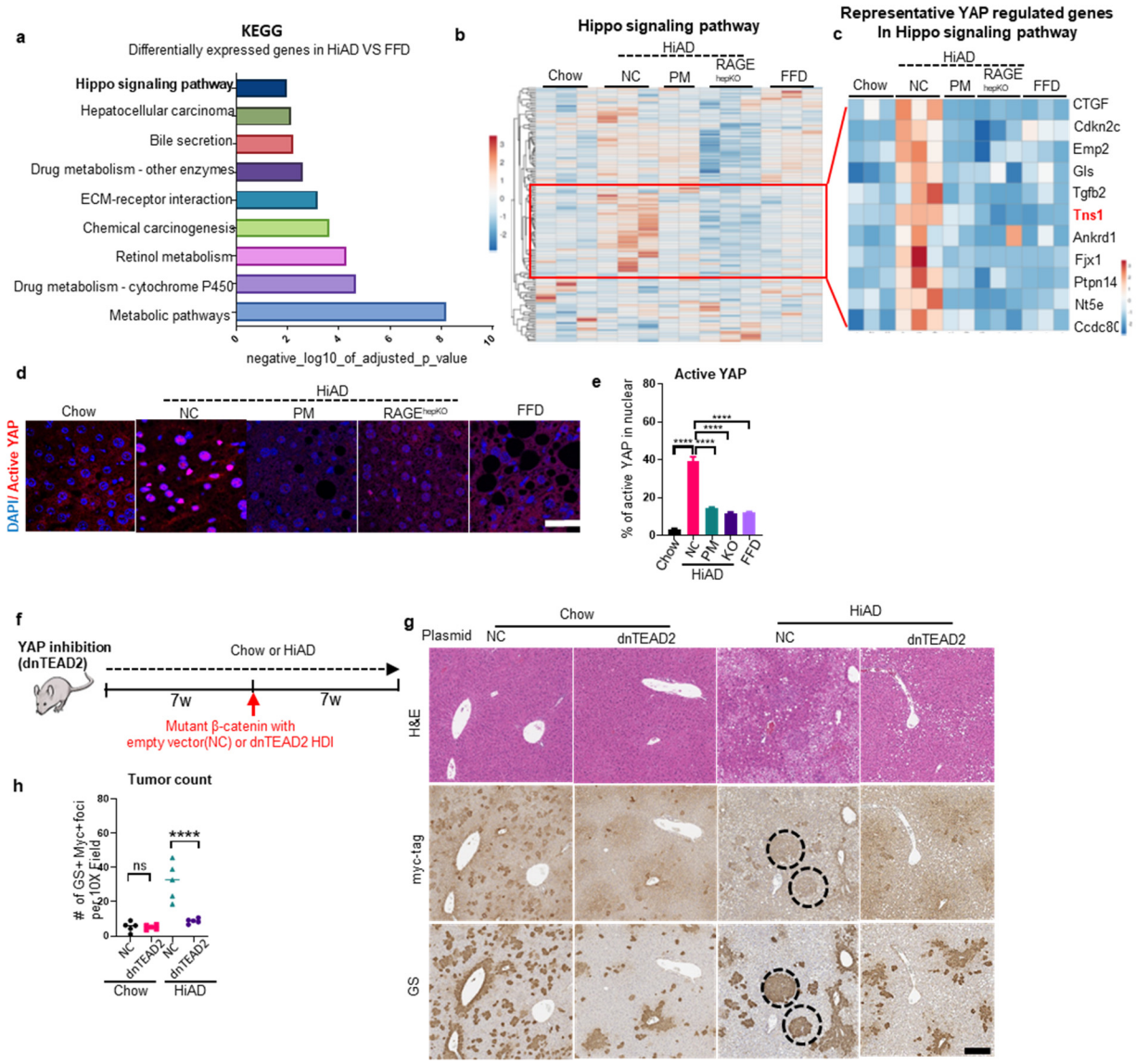

Fig. 4 YAP is involved in HCC growth driven by high viscoelasticity.

a-c. Analyses of bulk RNA-seq data from mice fed chow, FFD, and HiAD diets. Mice on HiAD were treated with PM injection and a group of mice with RAGE hepatocyte depletion ($RAGE^{HepKO}$) was studied. KEGG analysis (**a**) and heatmap **(b, c**) from RNAseq data show enrichment in several YAP/TAZ target genes in HiAD-fed mice, compared to the other groups. 2-3 samples from each groups were analyzed. No HD injection was done in these experiments. Genes with Log2 fold change (Log2FC) and p-value less than 0.05 were considered differentially expressed.

d, e. Representative images (**d**) and quantification(**e**) of active nuclear YAP signal in mouse livers. (n= 5 mice/group, 4 random ×20 fields/sample; data are presented as the percentage of active YAP/area/×20 field, NC: vehicle treated mice; ****P < 0.0001, ANOVA, post-hoc Tukey test).

f. Schematic presentation of the NASH-related HCC model combined with YAP inhibition. Mice were fed for 7 weeks chow or HiAD. HDI was performed using pT3-EF5a-hMet-V5 and pT3-EF5a-S45Yb-catenin-myc, with the sleeping beauty (SB) transposase at a ratio of 25:1. These mice were also co-injected with dominant-negative (dn) TEAD2, or control (empty vector). 7 weeks after HDI, mice were sacrificed and the livers analyzed.

g, h. H&E staining and GS/myc immunohistochemistry depict colocalization (**g**) and quantification (**h**) of GS/myc by immunohistochemistry showing an increase in double positive foci in control vector injected mice. Less foci were seen in those with dn TEAD2. Scale bar, 300 μm. (N=5, mean ± SEM; ****P < 0.0001, ns not significant, ANOVA, post-hoc Tukey test)

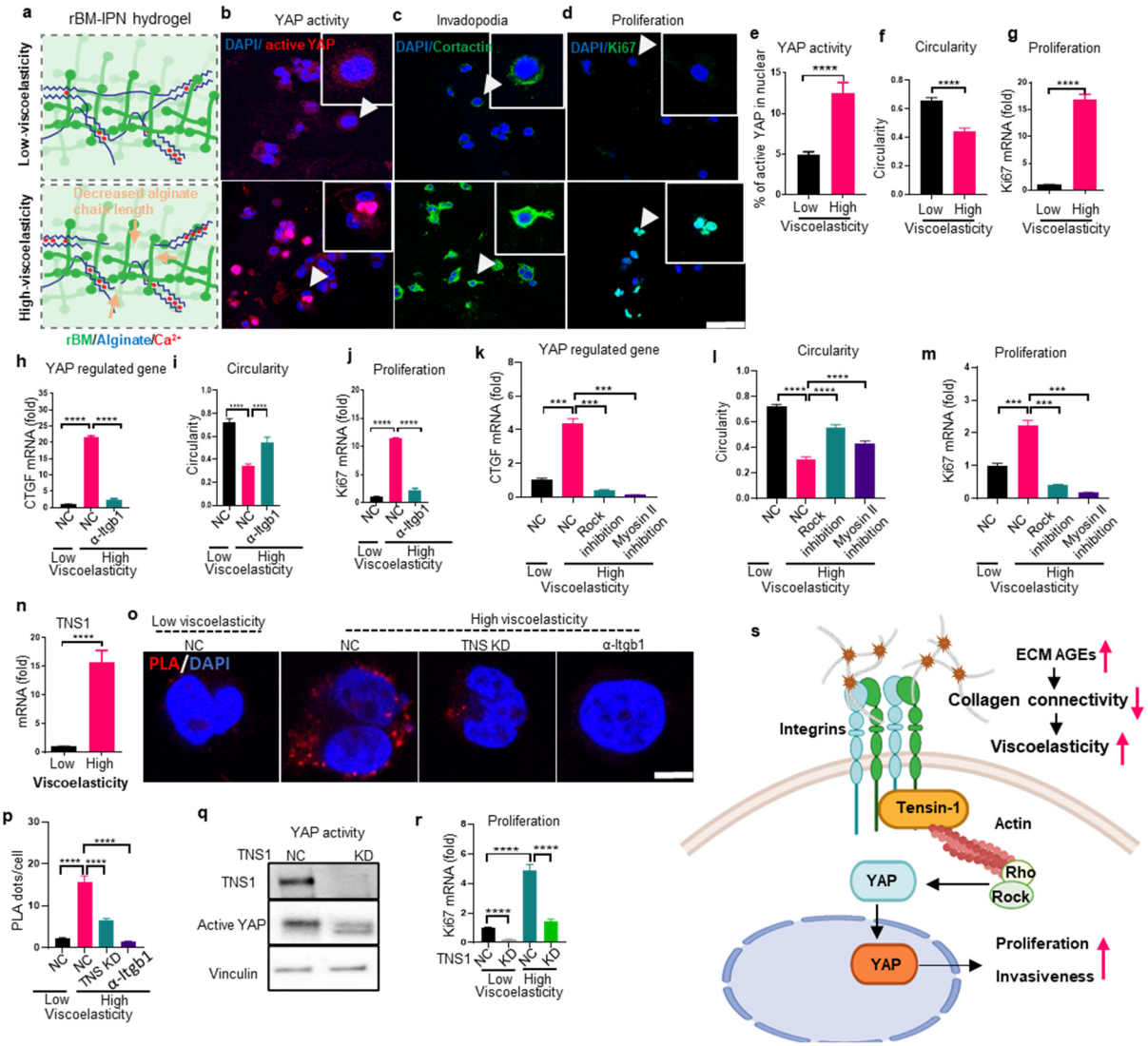

Fig. 5 Integrin β1 -Tensin 1-YAP axis mediates viscoelasticity-specific mechano-cellular pathways for HCC cell invasion

a. Schematics of the tunable viscoelasticity IPNs of alginate (blue) and reconstituted basement membrane (rBM) matrix (green) hydrogels. Lowering the molecular weight (MW) of alginate polymers (blue) crosslinked by calcium (red) decreases connectivity (orange arrows) of the network to increase the viscoelasticity.

b-g. After 1 day in 3D culture in low or high viscoelasticity hydrogels, YAP activity was analyzed using active YAP immunofluorescence (**b**), quantification (**e**). Invadopodia formation (immunofluorescence for cortactin) (**c**) and circularity analysis (image J) (**f**). Cell proliferation was

evaluated by Ki67 staining (**d**) and mRNA expression (**g**). Scale bar is 50 μm. (N=3, mean ± SEM; ****P < 0.0001, ANOVA, post-hoc Tukey test)

h-j. Huh7 cells encapsulated in low or high viscoelasticity IPN hydrogels were incubated with control IgG or integrin β1 blocking antibody. YAP activity was analyzed by testing YAP-regulated target gene CTGF mRNA expression (**h**). Invadopodia formation was analyzed by immunofluorescence for cortactin and cell circularity analysis (image J) (**i**). Cells proliferation was evaluated by Ki67 mRNA expression (**j**). (N=3, mean ± SEM; ****P < 0.0001, ANOVA, post-hoc Tukey test)

k-m. Huh7 cells encapsulated in low or high viscoelasticity IPN hydrogels were incubated with ROCK or Myosin II inhibitors. YAP activity was analyzed by testing YAP-regulated target gene CTGF mRNA expression (**k**). Circularity was analyzed (**l**), and cells proliferation was evaluated by Ki67 mRNA expression (**m**). (N=3, mean ± SEM; ****P < 0.0001, ANOVA, post-hoc Tukey test).

n. Tensin 1 (TNS1) mRNA expression in Huh7 cells cultured in variable viscoelasticity 3D hydrogels, analyzed by RT-qPCR. TNS-1 mRNA is induced in high viscoelasticity conditions.(N=3, mean ± SEM; ****P < 0.0001, post-hoc Tukey test)

o, p. Proximity ligation assay (PLA) analyses depict the direct binding between TNS1 and integrin β1 in high viscoelasticity 3D hydrogels. TNS1 knock-down or integrin β1 blocking reduced the interaction. PLA positive dots were quantified from 30 cells in 3 gels, each group.(mean ± SEM; ***p<0.001, ****P < 0.0001, ANOVA, post-hoc Tukey test)

q. Western blot of active YAP in Huh7 cells cultured in high viscoelasticity hydrogels. Crips/Cas9-mediated TNS1 knock-down decreased active YAP expression.

r. Huh7 cell proliferation was evaluated by Ki67 mRNA expression in low or high viscoelasticity 3D hydrogels with or without TNS1 knock-down, proliferation was reduced after TNS1 KD.

s. Schematic presentation of TNS1 that serves as a key component of the ECM mechano-sensor complex by binding to integrin β1 in high viscoelasticity ECM conditions. The illustration was created using BioRender.com.

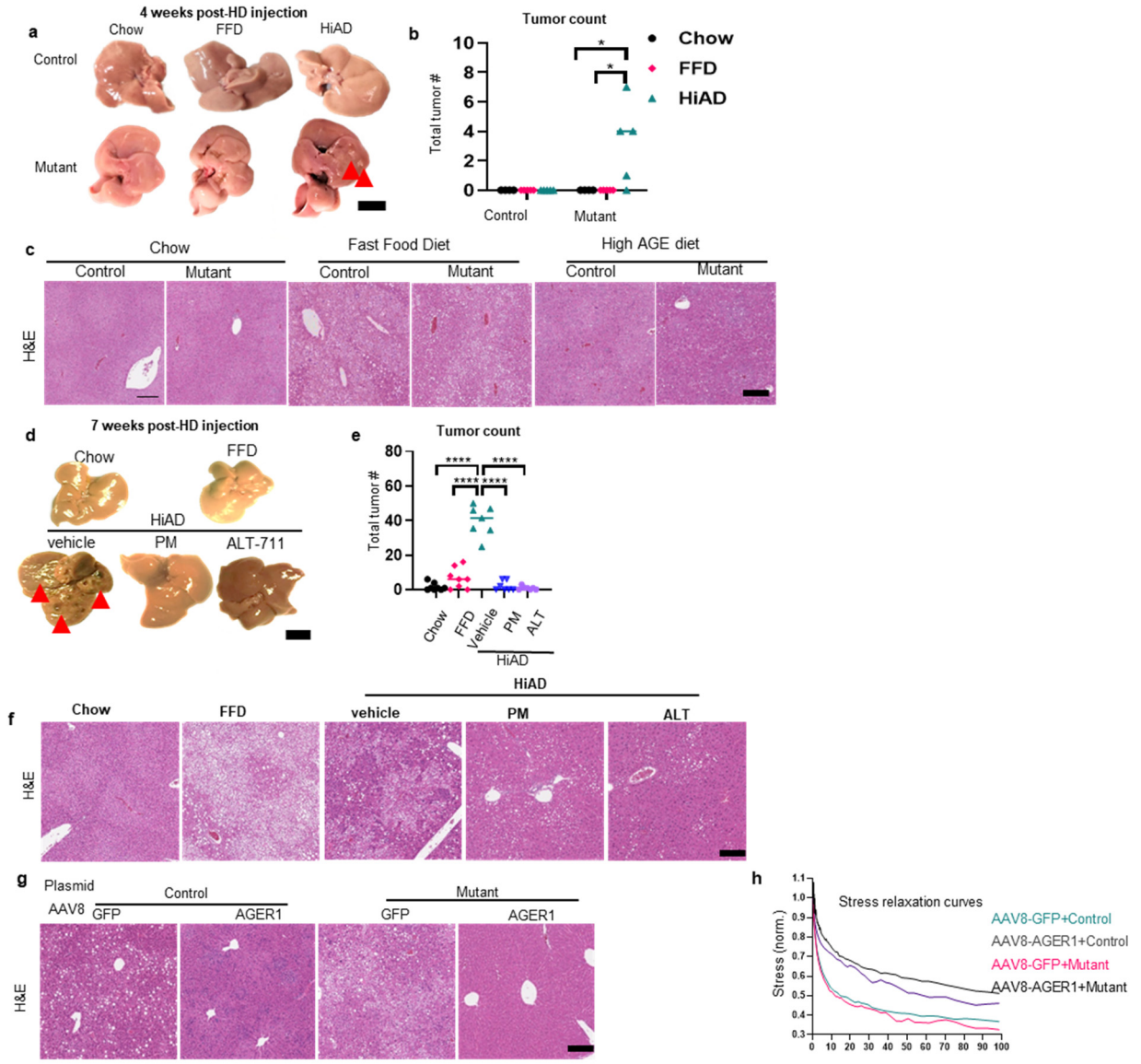

Extended Data Fig. 1 Mice on HiAD develop earlier and more numerous tumor foci following hydrodynamic injection, and exhibit AGEs-dependent higher viscoelasticity (related to main Figure 2)

a-c. Additional data of the early time point (4w post HDI) NASH/HCC model. Livers from Chow, FFD and HiAD-fed mice after HDI. Arrowheads, small lesions. Scale bar, 1cm(**a**). Quantification of visible liver tumors after 4 weeks of HDI (**b**). Hematoxylin and eosin (H&E) staining of the liver tissue, corresponding to GS/myc in the main figure. Scale bar, 300 μm (**c**). (n=5, mean ± SEM; *p<0.05, ANOVA)

d-f. Additional data of 7 weeks post-HD injection of the NASH/HCC model. Representative images (**d**) and quantification (**e**) of livers with visible liver tumors from mice after HDI. Arrowheads, tumors. Scale bar, 1cm. Hematoxylin and eosin (H&E) staining of liver tissue, corresponding to GS/myc in the main figure. Scale bar, 300 μm (**f**). (N=6-8, mean ± SEM; ****P < 0.0001, ANOVA, post-hoc Tukey test).

g, h. Additional data of NASH-related HCC model combined with AAV8-mediated AGER1 induction. H&E staining (**g**) of the liver tissue, corresponding to GS/myc in the main figure. Scale bar, 300 μm. Representative stress relaxation (**h**) curves with or without AGER1 induction.

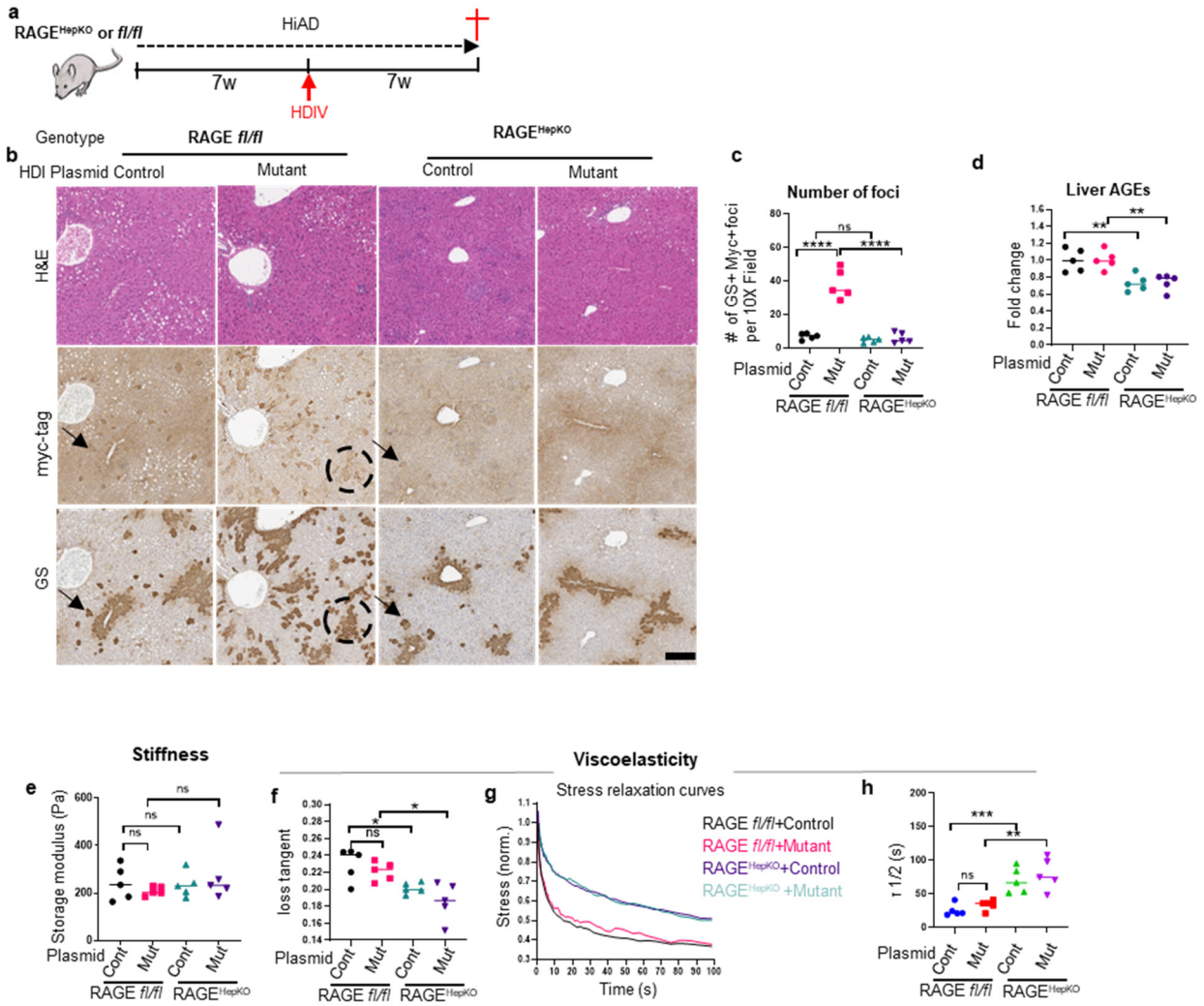

Extended Data Fig. 2 RAGE depletion in hepatocytes reverses fast stress relaxation in HiAD, and appearance of transformed foci.

a. Schematic presentation of the NASH-related HCC model combined with hepatocyte-specific RAGE deletion (RAGE^{HepKO}). HDI was performed using hMet/SB transposase with wild-type (control) or mutant β-catenin. **b.** H&E staining and GS/myc immunohistochemistry were performed, circles represent foci, arrows indicate transduced cells. Scale bar, 300 μm. **c.** Quantification of foci (N=5, mean ± SEM; ****P < 0.0001, ns not significant, ANOVA, post-hoc Tukey test). **d.** Liver AGEs were lower in RAGE^{HepKO} in mice. (n=5, mean±SEM, **P < 0.01, ANOVA). **e-g**. Liver stiffness (**d**) and viscoelasticity (**e-g**) were measured by rheometry. There was no significant difference in stiffness, but improved viscoelasticity in RAGE^{HepKO} mice. (N=5, mean ± SEM; *p<0.05, **p<0.01, ***p<0.001, ns not significant, ANOVA, post-hoc Tukey test).

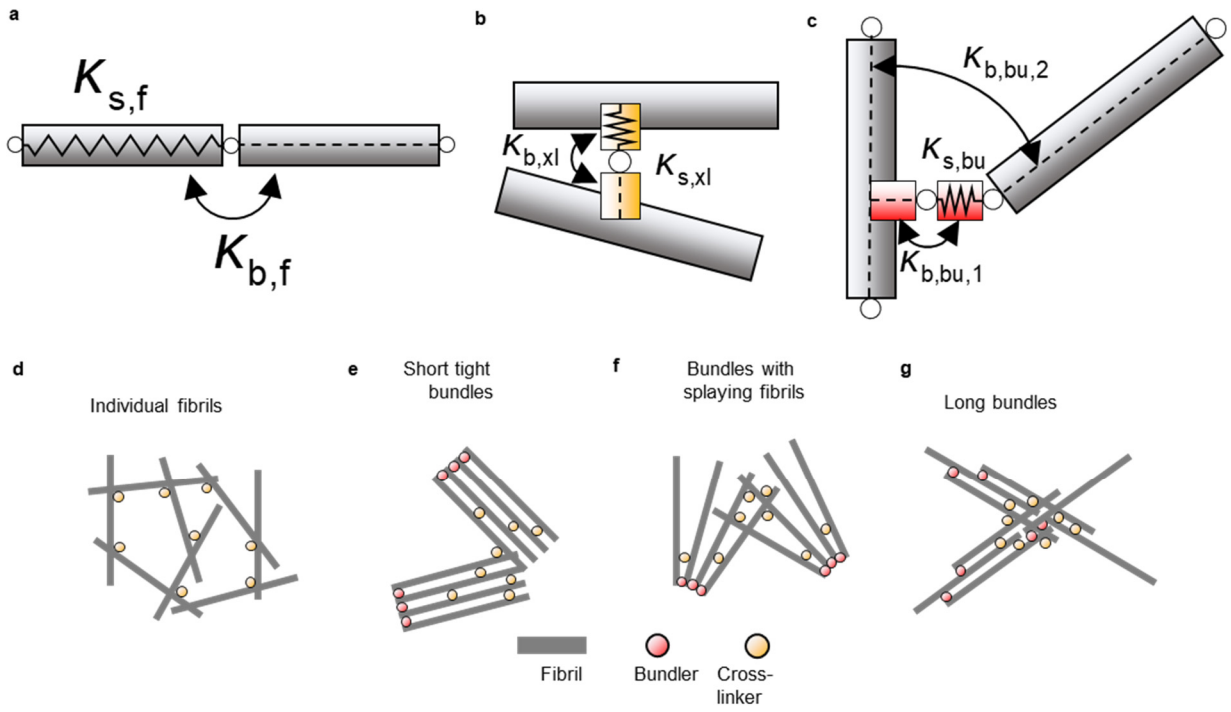

Extended Data Fig. 3: Agent-based computational model for a fibrillar matrix.

a-c. Fibrils (gray, "f"), cross-linkers (yellow, "xl"), and bundlers (red, "bu") are simplified by cylindrical segments in the model. Various bending (κ_b) and extensional (κ_s) stiffnesses maintain angles and lengths near their equilibrium values, respectively. Stiffnesses, equilibrium lengths, and equilibrium angles are listed in Table 4.

d-g. Different types of fibrils matrices. Without bundlers, a matrix is comprised of individual fibrils cross-linked to each other, resulting in small mesh size (**d**). With bundlers which bind only to the ends of fibrils, a matrix consists of short bundles. Depending on the angle between fibrils connected by bundlers, the shape of short bundles varies (**e, f**). With bundlers binding to the mid of fibrils, a matrix consists of longer bundles (**g**).

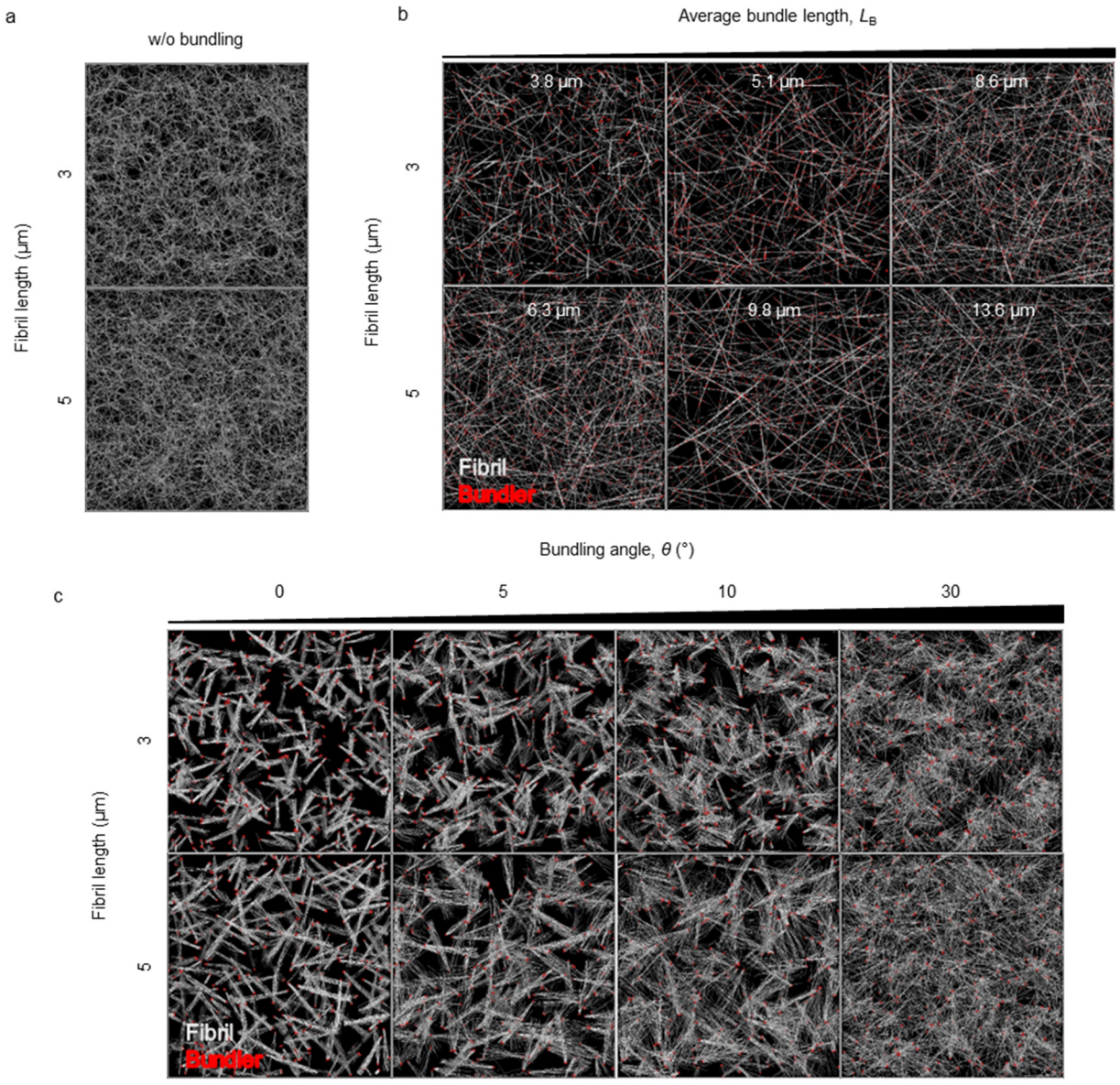

Extended Data Fig. 4: Snapshots of matrices employed for rheological measurements.

a. Matrix structures without bundlers.

b. Matrix structures with different bundle length.

c. Matrix structures with different bundling angles, θ. In all snapshots, white and red indicate fibrils and bundlers, respectively, and the length of fibrils is (top row) 3 μm or (bottom row) 5 μm.

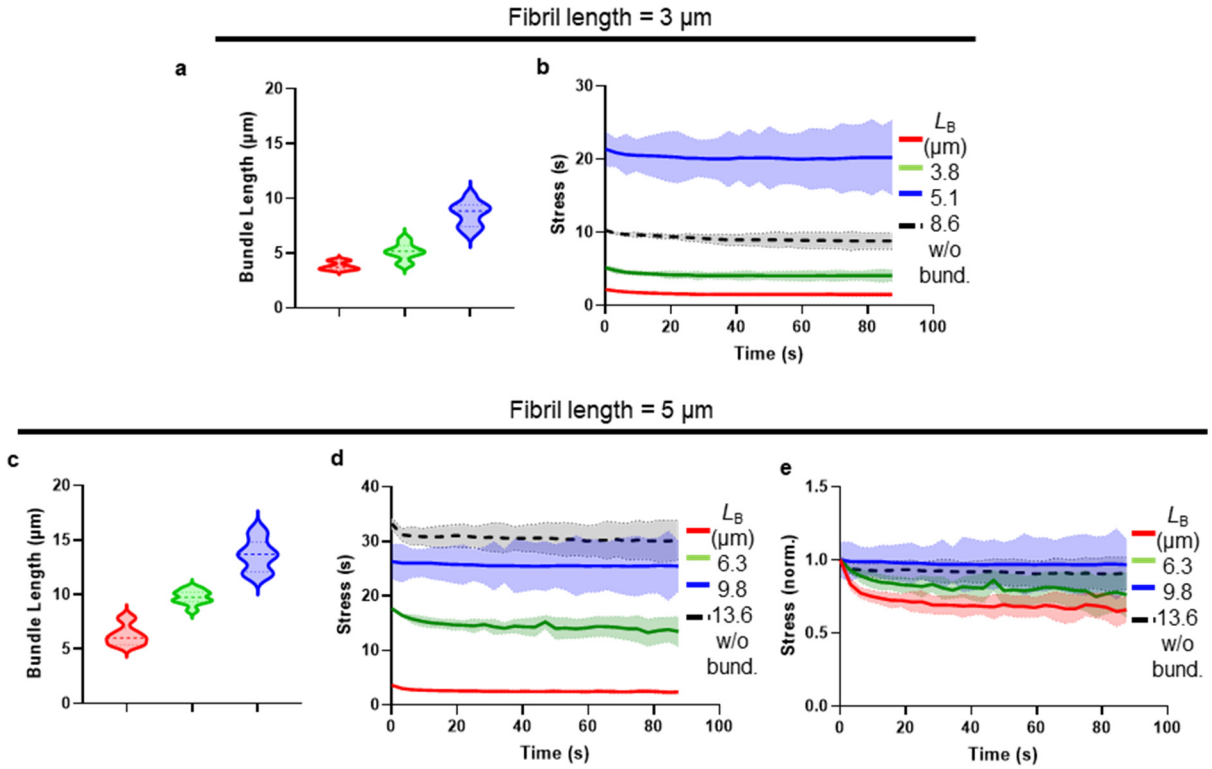

Extended Data Fig. 5: Stress relaxation in matrices with different bundle lengths, L_B.

a, b. Bundle length distribution and stress relaxation without normalization in the cases shown in Fig. 3s.

c-e. Bundle length distribution and stress relaxation with fibril length equal to 5 μm. Faster stress relaxation is observed in matrices consisting of smaller bundles.

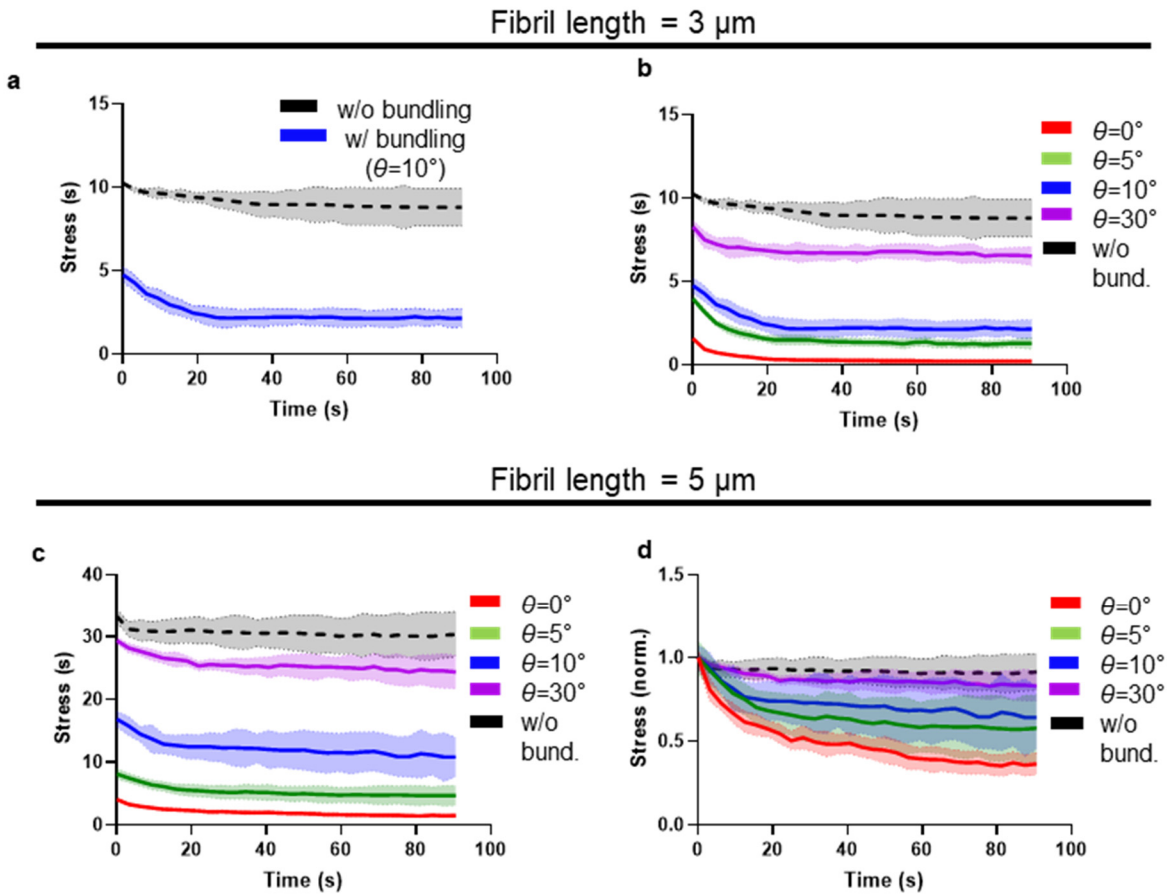

Extended Data Fig. 6: Stress relaxation in matrices generated with different bundling angles, *θ*.

a. Stress relaxation without normalization in the two representative cases shown in Fig. 3r.

b. Stress relaxation without normalization in the cases shown in Fig. 3t. In **a** and **b**, the length of fibrils is 3 μm.

c, d. Stress relaxation in cases with fibrils whose length is 5 μm.

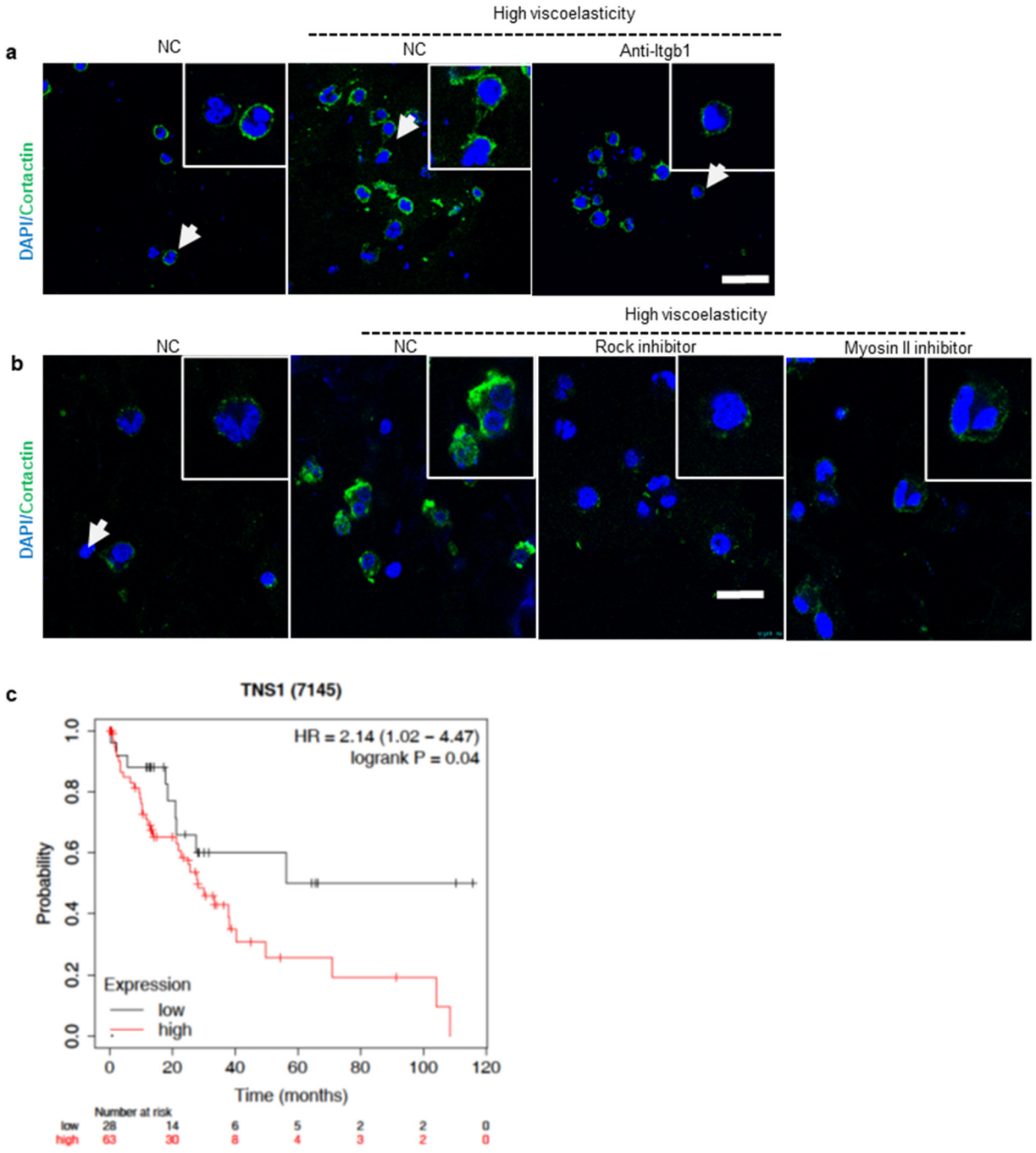

Extended Data Fig. 7: Additional data for Huh7 cell 3D culture hydrogel with variable viscoelasticity (related to main Figure 5)

a. Huh7 cells encapsulated in low or high viscoelasticity IPN hydrogels were incubated with control IgG or integrin β1-blocking antibody. Invadopodia formation was analyzed by immunofluorescence for cortactin (**a**). Scale bar is 50 μm.

b. Huh7 cells encapsulated in low or high viscoelasticity IPN hydrogels were incubated with ROCK or myosin II inhibitors. Invadopodia formation was analyzed by immunofluorescence for cortactin (**b**). Scale bar is 50 μm.

c. Kaplan-Meier (https://kmplot.com/analysis/) survival curve depicts that high expression of TNS1 correlated with worse survival in patients with HCC (non-viral and non-alcoholic etiology).

Materials and Methods

Human Liver Tissues

All human samples were de-identified and exempted (Exemption 4). Human liver samples were obtained from Stanford Diabetes Research Center (SDRC), Donor Network West (DNW) and Stanford Tissue Bank. Histology was evaluated for necroinflammation, hepatocellular ballooning, ductular reaction, and fibrosis by a hepato-pathologist in a blinded fashion, and NAS scores were provided. Detailed information about the donors, including sex, age, diagnosis, and NAS score, are summarized in Table 1.

Animal Studies

All animal experiments were conducted according to the experimental procedures approved by the Institutional Animal Care and Use Committee at Stanford University and Palo Alto VA. Mice were housed in standard cages with 12:12 hour light/dark cycles and *ad libitum* access to water and food unless otherwise indicated. Mice were placed on control chow, or fast-food diet (FFD) (17.4% protein, 20% fat, and 49.9% carbohydrate, AIN-76A) supplemented with high fructose corn syrup in the drinking water at a final concentration of 42 g/L for up to 14 weeks, or high AGEs diet (prepared by cooking FFD at 120°C for 20 minutes) as previously described [44] supplemented with high fructose water. Wildtype C57BL/6J (WT) 8- to 10-week-old male mice were purchased from the Jackson Laboratory. $Rage^{fl/fl}$ mice on a C57B6 background were gifted by Dr. B. Arnold from German Cancer Research Center, Heidelberg, Germany. $Rage^{HepKO}$ mice were generated by crossing $Rage^{fl/fl}$ mice with *Albumin-cre* mice (the Jackson Laboratory) for several generations. To generate hepatocyte transgenic AGER1 mice, WT mice were injected with adeno-associated virus 8 (AAV8)-control green fluorescent protein (AAV8-control) or AAV8-thyroxine-binding globulin-AGER1 recombinase (AAV8-AGER1) ($5x10e^{11}$ genome copies, Vector BioLabs) at week 6th of feeding (the rationale of the specific targeting in hepatocyte has been previously reported) [45]. To study the inhibition of AGEs formation or AGEs-protein crosslinking, WT mice fed with high AGEs diet were injected intraperitoneally daily with pyridoxamine hydrochloride (PM) (Sigma Aldrich) (60 mg/kg) [46], or alagebrium (ALT-711) (Sigma Aldrich, 1mg/kg)[47,48], or vehicle (Tris-HCl) from the 6th week of feeding. At the time of sacrifice, pictures of livers were taken, and the number and the size of tumors on the surface were recorded.

Hydrodynamic Tail Vein Injection and Plasmid Preparation

Oncogenic plasmids were delivered to the mouse liver by hydrodynamic tail vein injection as previously described[49]. In short, pT3-EF1α-h-hMet, pT3-EF1αh-wt-β-catenin-myc-tag, pT3-EF1α-h-s45y-mutant-β-catenin-myc-tag, and pCMV/ sleeping beauty transposase (SB) were constructed by Satdarshan P.S. Monga's lab. Plasmids used for in vivo experiments were purified using the Invitrogen Endotoxin-free Maxi prep kit (Sigma-Aldrich). A combination of 20 μg of pT3-EF5-hMet and 20 μg of pT3-EF5α-wt-b-catenin-myc or pT3-EF5α-S45Y-b-catenin-myc, along with 1.6 μg of SB (25:1) were diluted in 1 ml of endotoxin-free saline (AdipoGen), filtered through 0.22 mm filter (Millipore), and injected into the tail vein of mice in 5 to 7 seconds at the beginning of the 8th week of chow, FFD or HiAD feeding. To inhibit YAP activity, mice were injected with dominant negative (dn) TEAD2 (pT3-EF1α-h-dnTEAD2, 60μg)[50] or negative control vector (empty pT3-EF1α, 60 μg), (constructed by Satdarshan P.S. Monga's lab) by hydrodynamic tail vein injection at the beginning of the 8th week of chow or HiAD feeding with hMet, s45y-mutant-β-catenin, and SB.

Histology, Immunohistochemistry, and Early Foci Quantification

Paraffin-embedded tissue samples were cut into 5 μm sections, deparaffinized, and rehydrated. For antigen retrieval, slides were boiled in citrate buffer (0.01 M, pH 6.0) using a microwave oven on high power for 5 min and cooled down to room temperature. After incubation in 3% aqueous H_2O_2 to quench the endogenous peroxidase, sections were washed in PBST (PBS with 0.1% Tween 20, v/v) washing buffer, blocked with 5% goat serum (EMD Millipore) diluted in PBST at RT for 1 h, and incubated with primary antibody (Table 2) diluted in 2% goat serum in PBST at 4°C overnight.

For immunohistochemistry, slides were incubated with appropriate biotinylated secondary antibodies (Table 2) for 1 h, then processed according to the ABC Peroxidase Standard Staining Kit (Thermo) for 30 min. The slides were stained with 3, 3' Diaminobenzidine (Abcam) for 5 seconds (sec) to 5 min and counterstained with hematoxylin (Thermo) for 45 sec. Images were scanned with Leica Aperio AT2 at Stanford Human Pathology /Histology Service Center. Serial sections were incubated with GS and myc tag primary antibodies, and a cluster of cells (at least 20 cells) positive both for GS- and myc tag- positive were counted as early foci.

Measurement of AGEs content

The amount of AGEs was measured by OxiSelect™ Advanced Glycation End Product Competitive ELISA Kit (Cell Biolabs) in the serum and the liver homogenate, per the manufacturer's instructions. Briefly, 10 mg liver samples were homogenized in PBS. After measuring protein concentration, 300 µg protein were added to a 96-well ELISA plate and incubated for one hour at room temperature. Following incubation with the secondary HRP conjugated anti-AGEs, the reaction was halted with a stop solution, and the plates were read at 450 nm.

RNA Extraction, Reverse Transcription, and Real-time Quantitative Polymerase Chain Reaction (RT-qPCR)

According to the manufacturer's recommendations, total RNA was extracted from snap-frozen liver tissue and cells using an RNeasy mini kit (Qiagen). Complementary cDNA was created from an identical amount of RNA using the iScriptTM cDNA synthesis kit (Bio-Rad). The PowerUp SYBR Green PCR Master Mix (Applied Biosystems) was used for RT-qPCR on the 7900HT machine (Applied Biosystems), and the data were evaluated using the 2-Ct technique. As an endogenous control, acidic ribosomal phosphoprotein (Arbp) was used to standardize the data. The primer sequences used in this study are listed in Table 3.

Atomic Force Microscopy

Measurements on frozen liver tissues were performed on livers embedded in OCT compound (Sakura), snap frozen via direct immersion into liquid nitrogen, and cut into 100 µm sections on a Leica CM1900-13 cryostat. Samples were kept in a protease inhibitor cocktail during the AFM analysis (Roche Diagnostic). A Bruker BioAFM Resolve was used to take measurements (Bruker). For the indentation, Novascan Tech modified silicon nitride cantilevers (k = 0.01 N/m) with a 10 µm diameter borosilicate glass spherical tip were employed.

For each session, cantilevers were calibrated using the thermal oscillation method. AFM force maps were performed on 100 µm×100 µm fields. Each experimental group included at least 3

different mice, with 2 sections from each mouse, and 3 different areas generated per section. Data analyses were done using the Hertz model in NanoScope Analysis V1.9.

Rheometry for human and mouse livers

Measurements were optimized to assess storage modulus, loss modulus, loss tangent, and stress relaxation together based on the method previously described[51]. Briefly, liver samples were prepared using an 8 mm diameter punch (Integra Miltex). The height of the slices ranged from 3 to 5 mm in the uncompressed state. Samples were kept hydrated during all experiments with DMEM. Parallel plate shear rheometry was carried out on an ARES-G2 rheometer (TA instruments) at room temperature using TA TRIOS software (TA instruments). For all measurements, the upper plate was initially lowered to touch the sample, and 0.01N of nominal initial force (~300 Pa) was applied to ensure adhesive contact of the sample with the plates. Measurements were taken first with a dynamic time sweep test (2% constant strain, oscillation frequency 1radian/s, measurements taken for 600s), then stress relaxation (10% initial strain, measurements taken for 600s).

Measurement of total and insoluble collagen

Hydroxyproline assay for total liver collagen was performed as previously described[52]. Briefly, liver samples were homogenized and denatured in 6 N HCl. Hydrolyzed samples were then dried and washed three times with deionized water, followed by incubation in 50 mM chloramine T oxidation buffer for 20 min at room temperature. The samples were incubated with 3.15 M perchloric acid (Sigma-Aldrich) for 5 min, then with p-dimethylaminobenzaldehyde (Sigma-Aldrich). The absorbance of each sample was measured.

For insoluble collagen, the liver or collagen gel was first homogenized in 0.5M Acetic Acid with a 1:4 ratio (ex 800 ul for 200 mg liver) to make 20% liver homogenate. Next, 500ul of 20% liver homogenate was added onto 1ml of 0.5M Acetic Acid and tubes rotated at 4°C overnight. Samples were centrifuged at 20000g for 30min to collect the pellet, resuspended in pepsin (2 mg/ml in 0.5M Acetic Acid) and incubated at 4°C overnight. Next day the samples were centrifuged and the pellets collected. These were then studied by the Hydroxyproline Assay, described previously.

Preparation of AGEs-BSA

AGEs-BSA were prepared as previously described [53,54]. Briefly, glycolaldehyde (Sigma-Aldrich) was dissolved in 10 mg/ml BSA/PBS to a final concentration of 33 mM. The solutions were incubated at 37°C for 72 h, followed by dialysis against PBS. The dialyzed solutions were sterilized with 2 μM filters, and aliquots were stored at -80°C.

Preparation of AGEs-modified collagen and gels

Collagen type I (Corning) was incubated with 2.5mg/ml in AGEs-BSA 0.1% acetic acid (Merck) to obtain 3 mg/mL collagen solution days at 4 °C for 4 weeks. BSA was mixed with collagen as the control. Alagebrium chloride (ALT, 20 mg/ml) was added as the AGEs crosslinking inhibitor. Collagen gels were polymerized by mixing 3 mg/mL AGEs modified or non-modified collagen solution with 10×PBS and neutralized with 1× NaOH (Merck) and incubated at 37 °C for 90 min leading to the formation of gels. For most gels, 1.6 mg/ml collagen was used.

Alginate preparation

According to the manufacturer, low-molecular-weight, ultra-pure sodium alginate (Provona UP VLVG, NovaMatrix), with a molecular weight (MW) of <75 kDa was used for fast-relaxing substrates. For slow-relaxing substrates, sodium alginate with a high MW and a concentration of guluronic acid blocks was utilized (FMC Biopolymer, Protanal LF 20/40, High-MW, 280 kDa). Alginate was treated with activated charcoal, dialyzed against deionized water for 3–4 days (MW cut-off of 3,500 Da), sterile-filtered, lyophilized, and then reconstituted to 3.5 wt% in serum-free DMEM (Gibco).The use of low/high-MW alginate resulted in high/low viscoelasticity IPNs.

Imaging for collagen fibrils

Methods were previously described for collagen fibrils in the liver [55]. Briefly, mouse livers were decellularized in situ by detergent (0.5% (wt/vol) sodium deoxycholate, 250mL/mouse) and water (50 mL/mouse) perfusion at a pump speed of 0.2 ml/min. After the final perfusion, the livers were removed and washed overnight in PBS. For AGEs-modified collagen gels, samples were prepared as previously described. Gels were imaged 1 day after formation.

For second harmonic generation (SHG) imaging, all samples were imaged using a Leica TCS SP5 multiphoton confocal microscope, and a 20×, HC PL Apo, NA 0.7 oil-immersion objective was used throughout the experiments. The excitation wavelength was tuned to 840 nm, and a 420 ± 5 nm narrow bandpass emission controlled by a slit was used for detecting the SHG signal of collagen. The images are recorded with an inverted confocal laser scanning microscope (Leica TCS SP8) equipped with a 20× water-immersion objective for confocal reflection imaging. An Ar+ laser at 488 nm was used to illuminate the sample, and the reflected light is detected with photomultiplier tube (PMT) detectors. Scans were 1024 × 1024 pixels, and all images are taken 80–100 μm into the samples. Collagen measurements were performed using CT-Fire software (v.2.0 beta) (https://loci.wisc.edu/software/ctfire) and ImageJ (https://imagej-nih-gov.stanford.idm.oclc.org/ij/).

Interpenetrating polymer network (IPN) 3D hydrogels formation

Alginate was transferred to a 1.5 ml Eppendorf tube (a polymer tube) and kept on ice for each viscoelastic gel. For rBM-IPNs, alginate was mixed 30 times before the addition of rBM (Corning), at 4ºC. Collagen-IPNs were created by diluting and neutralizing AGEs modified or unmodified collagen gels with 10 DMEM and 1 NaOH (Merck) at 4ºC. All substrates had a final concentration of 10 mg/ml alginate, 4.4 mg/ml rBM, or 1.6 mg/ml collagen after additional DMEM was added. This was pipette-mixed, and the resulting concoction was kept on ice. Calcium sulfate was added to 1 ml Luer lock syringes (Cole-Parmer) and stored on ice to maintain the constant Young's moduli of the substrates with high and low viscoelasticity. The polymer mixes were divided into individual 1-ml Luer lock syringes (polymer syringes) and placed on ice as well. With care to avoid introducing bubbles or air into the mixture, the polymer syringe was linked to the calcium sulfate syringe to create gels. The two solutions were quickly combined using 30 pumps on the syringe handles, and the resulting mixture was placed into a well of an eight-well Lab-Tek plate (Thermo Scientific) that had been precoated with rBM. After moving the Lab-Tek dish to a 37 °C incubator, the gel was allowed to form for 1 hour before a full medium was added.

Mechanical characterization of IPNs

Rheology experiments were carried out with a stress-controlled AR2000EX rheometer (TA Instruments). IPNs were directly deposited onto the lower Peltier plate for rheology testing. The gel was then slowly contacted by a 25-mm flat plate, creating a 25-mm disk gel. To stop dehydration, mineral oil (Sigma) was applied to the gel's edges. The storage and loss moduli had equilibrated by the time the time sweep was done, which was at 1 rad/s, 37 °C, and 1% strain.

For the stress relaxation experiments, after the time sweep, a constant strain of 5% was applied to the gel at 37 °C, and the resulting stress was recorded over the course of 4 h.

Cell culture and Crisp/Cas9 mediated TNS1 knockdown

Human hepatocyte-derived cellular carcinoma cell line, Huh7, was cultured in high glucose DMEM (Gibco) with 10% fetal bovine serum (FBS) (Gibco) with 1% Pen/Strep (Life Technologies). All cells were cultured at 37 °C in 5% CO_2.

TNS1 was knocked down in Huh7 cells by using TNS1 sgRNA(sgRNA1, GTAGAACAACGACATTGTGA; sgRNA2, TGGCTACAAGACTCTCCAAG; sgRNA3, CCCAACTTTGAGTCTAAAGG). An irrelevant sgRNA sequence was used as a negative control. sgRNAs were cloned into vector pMCB306 (Addgen Plasmid #89360, sgRNA expression vector with GFP, puromycin resistance), then co-transfected to Huh7 cells with lentiCas9-Blast (Addgen Plasmid #52962, expresses human codon-optimized S. pyogenes Cas9 protein and blasticidin resistance from EFS promoter). Transfected cells were selected by puromycin and tested for TNS1 expression 2 days after transfection.

3D cell encapsulation in IPNs

For analysis of YAP activation, invadopodia formation, and proliferation, Huh7 cells were serum-starved overnight and encapsulated in IPNs. In brief, cells were washed with PBS, trypsinized using 0.05% trypsin/EDTA, washed once, centrifuged, and resuspended in serum-free medium. The concentration of cells was determined using a Vi-Cell Coulter counter (Beckman Coulter). After Matrigel was mixed with alginate, cells were added to this polymer mixture and deposited into a cooled syringe. The solution was then vigorously mixed with a solution containing $CaSO_4$ and deposited into wells of a chambered coverglass (LabTek). The final concentration of cells was

3×10^6 cells/m of IPN. The cell-laden hydrogels were gelled in an incubator at 37 °C and 5% CO_2 for 60 min and then were stimulated with a medium containing 10% FBS. After one day, cells were collected for RT-PCR, WB, and immunostaining analysis.

Inhibitors

Inhibitors were used in the 3D cell culture at the following concentrations: 10 μM Y-27632 to inhibit ROCK (Sigma); 50 μM Blebbistatin (Abcam); and 1 μg mL^{-1} monoclonal β1 integrin-blocking antibody (Abcam, P5D2). Vehicle-alone controls for these inhibitors were as follows: DMSO for Blebbistatin, and Latrunculin-a; deionized water for Y-27632; and IgG nonspecific antibody (Sigma, I5381) for β1 integrin-blocking antibody. Y-27632 and Blebbistatin were added to the culture medium directly. Integrin β1 -blocking antibody was incubated with Huh7 cells on ice for 1 hour before encapsulation in IPNs and added to the culture medium directly.

RNA Sequencing, Bioinformatics Analysis, and Kyoto Encyclopedia of Genes and Genomes (KEGG) Analysis

$Rage^{fl/fl}$ (WT) mice were subjected to chow, FFD, or HiAD for 14 weeks. A group of HiAD-fed mice was injected i.p. daily with PM. A cohort of $Rage^{HepKO}$ mice was placed on HiAD for 14 weeks as published [10]. RNA was prepared from three mice per each group, and RNA sequencing was performed at Novogene (USA). Gencode gene annotations version M18 and the mouse reference genome major release GRCm38 was derived from https://www.gencodegenes.org/. Dropseq tools v1.1249 were used for mapping the raw sequencing data to the reference genome. The resulting UMI-filtered count matrix was imported into R v3.4.4. Before differential expression analysis with Limma v3.40.650 sample-specific weights were estimated and used as coefficients alongside the experimental groups as a covariate during model fitting with Voom. T-test was used for determining differentially ($P<0.05$) regulated genes between all possible experimental groups. GSEA was conducted with the pre-ranked GSEA method within the MSigDB Reactome, KEGG, and Hallmark databases (https://broadinstitute.org/msigdb). Raw sequencing data will be uploaded to NCBI.

Protein Extraction and Western Blotting

Cells were washed with phosphate-buffered saline (PBS) and lysed with RIPA Buffer. The homogenate was centrifuged, and the supernatant was collected. Protein concentrations were determined with Pierce BCA Protein Assay Kit (Thermo). Protease inhibitor (Roche) and phosphatase inhibitor (Roche) were added to all the lysis procedures mentioned above, and 10-50 μg of the protein samples were loaded onto SDS-polyacrylamide gel. The proteins were transferred to a polyvinylidene difluoride membrane or nitrocellulose membrane, which was blocked with 5% BSA in TBST and then incubated with primary antibodies at 4°C (Table 2) overnight. The blots were washed with TBST and further incubated with horseradish peroxidase-conjugated secondary antibodies (Table 2). The signal was detected by adding Western-Bright enhanced chemiluminescence substrate (Advansta) or SuperSignal West Pico PLUS Chemiluminescent Substrate (Thermo) and imaged with film or iBright CL1500 imaging system (Thermo). The images were processed and analyzed with NIH ImageJ and iBright Analysis software (Thermo).

Fluorescent Immunostaining and Microscopy

Frozen sections of livers or gel-embedded cells were washed twice with PBS and fixed with 4% paraformaldehyde at 4°C overnight. Sections were permeabilized in PBS with 0.4% (v/v) Triton X-100 for 10 min. After blocking with 5% goat serum in PBST at RT for 1 h, cells were incubated with primary antibodies (Table 2) diluted in 2% goat serum in PBST at 4°C overnight. The slides were washed and then incubated with secondary antibodies (Table 2) at RT for 1 h. Coverslips were washed with PBST between incubations and mounted with an anti-fade mounting medium with DAPI. Fluorescent images were taken with Leica TCS SPE. Images were processed with NIH ImageJ. To quantify cell circularity and cell area, the confocal images of cells were analyzed in ImageJ (https://imagej-nih-gov.stanford.idm.oclc.org/ij/) to calculate circularity and cell area. Circularity, mathematically calculated as $4\pi \times \text{area} \times (\text{perimeter})^{-2}$, ranges from 0 to 1, with a value of 1 being a perfect circle.

Proximity Ligation Assay

Duolink Proximity Ligation assay kit (Sigma-Aldrich) was used to determine the interaction of TNS1 and integrin β1 in Huh7 cells. Reagents were used following the manufacturer's instructions, and steps were optimized. In brief, anti-TSN1 and anti-integrin β1 were used as primary antibodies. The primary antibodies bound a pair of oligonucleotide-labeled secondary antibodies (PLA probes), the hybridizing connector oligos joined the PLA probes if they were close by, and the ligase created the DNA template needed for rolling-circle amplification (RCA). By using confocal microscopy, labeled oligos hybridized to the complementary sequences in the amplicon and produced discrete red fluorescent signals that could be seen and measured. (Leica Microsystems Inc.). NIH Image J software was used to count the signal, and the average counts were used to plot the bar graph.

Simulation Modeling

In this study, we used an agent-based model for simulating the discrete structure of collagen matrices. Supplementary Table 4 describe the details of the model and all parameter values employed in the model. The computational domain is rectangular with 20×20×5 μm in x, y, and z directions. A periodic boundary condition exists only in x and z directions. In simulations, the motions of the cylindrical elements are updated at each time step via the Langevin equation and the Euler integration scheme. The matrix consists of either thin collagen fibrils or bundles that are interconnected by cross-linkers. Each bundle is comprised of several thin fibrils joined by bundlers. Fibrils are joined either at their ends to create short bundles or in a staggering manner to create longer bundles. The shape of short bundles varies depending on the angle between fibrils; they can be thick rod-shaped bundles or loose bundles with splaying fibrils. While the bundlers are permanently bound to fibrils, the cross-linkers can unbind from fibrils at a rate that exponentially increases with an increasing force, following Bell's law. Fibrils are permanently bound to two boundaries normal to the y direction (i.e., +y boundary located at y = 20 μm and – y boundary located at y = 0 μm). After completion of matrix assembly, 20% strain is applied to the +y boundary in the x direction, whereas the -y boundary is fixed. After reaching the 20% strain, the strain is held at a constant level to measure stress relaxation.

Statistical Analysis

Data are presented as mean ± standard error of the mean (SEM). Statistical analyses were performed with GraphPad Prism 9 (GraphPad Software) using ANOVA and unpaired *t* test with Welch's correction or Mann-Whitney test for non-parametric values. Normality distribution was assessed with the Kolmogorov-Smirnov test. A value of at least $p<0.05$ has been considered and stated as significant.

Acknowledgments

Patient samples were obtained using the services of the Diabetes Clinical and Translational Core facility of the Stanford Diabetes Research Center which is supported by the National Institute of Diabetes and Digestive and Kidney Diseases of the National Institutes of Health under Award Number P30DK116074. Research organization/authors hereby express its thanks for the cooperation of Donor Network West and all of the organ and tissue donors and their families, for giving the gift of life and the gift of knowledge, by their generous donation.

Part of this work was performed at the Stanford Nano Shared Facilities (SNSF), supported by the National Science Foundation under award ECCS-2026822. Part of this work was performed at Stanford Cell Sciences Imaging Facility(CSIF), supported by the Award Number 1S10OD010580-01A1 and S10RR02557401 from the National Center for Research Resources (NCRR). Its contents are solely the responsibility of the authors and do not necessarily represent the official views of the NCRR or the National Institutes of Health. We are grateful to Dr. Marcin Walkiewicz (Stanford SNSF) for the AFM, and to Dr. Jon Mulholland and Dr. Kitty Lee (Stanford CSIF) for the imaging.

This research was supported by funding from the NIDDK R01 2DK083283 (to NJT), NIA 1RO1AG060726 (to NJT), SPARK Program (Stanford University to NJT), I01 BX002418 (NJT) and NCI R37 CA214136 (to OC). The study was also funded in part by NIH grants 1R01CA251155 and 1R01CA204586 to SPM.

References:

1 Cox, T. R. The matrix in cancer. *Nat Rev Cancer* **21**, 217-238 (2021). https://doi.org:10.1038/s41568-020-00329-7

2 Piersma, B., Hayward, M. K. & Weaver, V. M. Fibrosis and cancer: A strained relationship. *Biochim Biophys Acta Rev Cancer* **1873**, 188356 (2020). https://doi.org:10.1016/j.bbcan.2020.188356

3 Schrader, J. *et al.* Matrix stiffness modulates proliferation, chemotherapeutic response, and dormancy in hepatocellular carcinoma cells. *Hepatology* **53**, 1192-1205 (2011). https://doi.org:10.1002/hep.24108

4 McGlynn, K. A., Petrick, J. L. & El-Serag, H. B. Epidemiology of Hepatocellular Carcinoma. *Hepatology* **73 Suppl 1**, 4-13 (2021). https://doi.org:10.1002/hep.31288

5 Negro, F. Natural history of NASH and HCC. *Liver international : official journal of the International Association for the Study of the Liver* **40 Suppl 1**, 72-76 (2020). https://doi.org:10.1111/liv.14362

6 Kramer, J. R. *et al.* Effect of diabetes medications and glycemic control on risk of hepatocellular cancer in patients with nonalcoholic fatty liver disease. *Hepatology* **75**, 1420-1428 (2022). https://doi.org:10.1002/hep.32244

7 Henning, C., Smuda, M., Girndt, M., Ulrich, C. & Glomb, M. A. Molecular basis of maillard amide-advanced glycation end product (AGE) formation in vivo. *The Journal of biological chemistry* **286**, 44350-44356 (2011). https://doi.org:10.1074/jbc.M111.282442

8 McVicar, C. M. *et al.* Role of the receptor for advanced glycation endproducts (RAGE) in retinal vasodegenerative pathology during diabetes in mice. *Diabetologia* **58**, 1129-1137 (2015). https://doi.org:10.1007/s00125-015-3523-x

9 Colhoun, H. M. *et al.* Total soluble and endogenous secretory receptor for advanced glycation end products as predictive biomarkers of coronary heart disease risk in patients with type 2 diabetes: an analysis from the CARDS trial. *Diabetes* **60**, 2379-2385 (2011). https://doi.org:10.2337/db11-0291

10 Dehnad, A. *et al.* AGER1 downregulation associates with fibrosis in nonalcoholic steatohepatitis and type 2 diabetes. *J Clin Invest* **130**, 4320-4330 (2020). https://doi.org:10.1172/JCI133051

11 Andriotis, O. G. *et al.* Hydration and nanomechanical changes in collagen fibrils bearing advanced glycation end-products. *Biomed Opt Express* **10**, 1841-1855 (2019). https://doi.org:10.1364/BOE.10.001841

12 Chaudhuri, O., Cooper-White, J., Janmey, P. A., Mooney, D. J. & Shenoy, V. B. Effects of extracellular matrix viscoelasticity on cellular behaviour. *Nature* **584**, 535-546 (2020). https://doi.org:10.1038/s41586-020-2612-2

13 Adebowale, K. *et al.* Enhanced substrate stress relaxation promotes filopodia-mediated cell migration. *Nat Mater* (2021). https://doi.org:10.1038/s41563-021-00981-w

14 Charrier, E. E., Pogoda, K., Wells, R. G. & Janmey, P. A. Control of cell morphology and differentiation by substrates with independently tunable elasticity and viscous dissipation. *Nat Commun* **9**, 449 (2018). https://doi.org:10.1038/s41467-018-02906-9

15 Nam, S. *et al.* Cell cycle progression in confining microenvironments is regulated by a growth-responsive TRPV4-PI3K/Akt-p27(Kip1) signaling axis. *Sci Adv* **5**, eaaw6171 (2019). https://doi.org:10.1126/sciadv.aaw6171

16 Wisdom, K. M. *et al.* Matrix mechanical plasticity regulates cancer cell migration through confining microenvironments. *Nat Commun* **9**, 4144 (2018). https://doi.org:10.1038/s41467-018-06641-z

17 Farrell, G. *et al.* Mouse Models of Nonalcoholic Steatohepatitis: Toward Optimization of Their Relevance to Human Nonalcoholic Steatohepatitis. *Hepatology* **69**, 2241-2257 (2019). https://doi.org:10.1002/hep.30333

18 Febbraio, M. A. *et al.* Preclinical Models for Studying NASH-Driven HCC: How Useful Are They? *Cell metabolism* **29**, 18-26 (2019). https://doi.org:10.1016/j.cmet.2018.10.012

19 Tao, J. *et al.* Modeling a human hepatocellular carcinoma subset in mice through coexpression of met and point-mutant beta-catenin. *Hepatology* **64**, 1587-1605 (2016). https://doi.org:10.1002/hep.28601

20 Naomi, R., Ridzuan, P. M. & Bahari, H. Current Insights into Collagen Type I. *Polymers (Basel)* **13** (2021). https://doi.org:10.3390/polym13162642

21 Gautieri, A. *et al.* Advanced glycation end-products: Mechanics of aged collagen from molecule to tissue. *Matrix Biol* **59**, 95-108 (2017). https://doi.org:10.1016/j.matbio.2016.09.001

22 Dandia, H., Makkad, K. & Tayalia, P. Glycated collagen - a 3D matrix system to study pathological cell behavior. *Biomater Sci* **7**, 3480-3488 (2019). https://doi.org:10.1039/c9bm00184k

23 Ban, E. *et al.* Mechanisms of Plastic Deformation in Collagen Networks Induced by Cellular Forces. *Biophysical journal* **114**, 450-461 (2018). https://doi.org:10.1016/j.bpj.2017.11.3739

24 Munster, S. *et al.* Strain history dependence of the nonlinear stress response of fibrin and collagen networks. *Proceedings of the National Academy of Sciences of the United States of America* **110**, 12197-12202 (2013). https://doi.org:10.1073/pnas.1222787110

25 Nam, S., Hu, K. H., Butte, M. J. & Chaudhuri, O. Strain-enhanced stress relaxation impacts nonlinear elasticity in collagen gels. *Proceedings of the National Academy of Sciences of the United States of America* **113**, 5492-5497 (2016). https://doi.org:10.1073/pnas.1523906113

26 Adebowale, K. *et al.* Enhanced substrate stress relaxation promotes filopodia-mediated cell migration. *Nat Mater* **20**, 1290-1299 (2021). https://doi.org:10.1038/s41563-021-00981-w

27 Blangy, A. Tensins are versatile regulators of Rho GTPase signalling and cell adhesion. *Biol Cell* **109**, 115-126 (2017). https://doi.org:10.1111/boc.201600053

28 Haynie, D. T. Molecular physiology of the tensin brotherhood of integrin adaptor proteins. *Proteins* **82**, 1113-1127 (2014). https://doi.org:10.1002/prot.24560

29 Hall, E. H., Daugherty, A. E., Choi, C. K., Horwitz, A. F. & Brautigan, D. L. Tensin1 requires protein phosphatase-1alpha in addition to RhoGAP DLC-1 to control cell polarization, migration, and invasion. *The Journal of biological chemistry* **284**, 34713-34722 (2009). https://doi.org:10.1074/jbc.M109.059592

30 Elosegui-Artola, A. *et al.* Mechanical regulation of a molecular clutch defines force transmission and transduction in response to matrix rigidity. *Nat Cell Biol* **18**, 540-548 (2016). https://doi.org:10.1038/ncb3336

31 Engler, A. J., Humbert, P. O., Wehrle-Haller, B. & Weaver, V. M. Multiscale modeling of form and function. *Science* **324**, 208-212 (2009). https://doi.org:10.1126/science.1170107

32 Escala-Garcia, M. *et al.* Breast cancer risk factors and their effects on survival: a Mendelian randomisation study. *BMC medicine* **18**, 327 (2020). https://doi.org:10.1186/s12916-020-01797-2

33 Soltani, G. *et al.* Obesity, diabetes and the risk of colorectal adenoma and cancer. *BMC Endocr Disord* **19**, 113 (2019). https://doi.org:10.1186/s12902-019-0444-6

34 Tsilidis, K. K., Kasimis, J. C., Lopez, D. S., Ntzani, E. E. & Ioannidis, J. P. Type 2 diabetes and cancer: umbrella review of meta-analyses of observational studies. *Bmj* **350**, g7607 (2015). https://doi.org:10.1136/bmj.g7607

35 Wojciechowska, J., Krajewski, W., Bolanowski, M., Krecicki, T. & Zatonski, T. Diabetes and Cancer: a Review of Current Knowledge. *Exp Clin Endocrinol Diabetes* **124**, 263-275 (2016). https://doi.org:10.1055/s-0042-100910

36 Andersen, D. K. *et al.* Diabetes, Pancreatogenic Diabetes, and Pancreatic Cancer. *Diabetes* **66**, 1103-1110 (2017). https://doi.org:10.2337/db16-1477

37 Yamauchi, M., Barker, T. H., Gibbons, D. L. & Kurie, J. M. The fibrotic tumor stroma. *J Clin Invest* **128**, 16-25 (2018). https://doi.org:10.1172/JCI93554

38 Levental, K. R. *et al.* Matrix crosslinking forces tumor progression by enhancing integrin signaling. *Cell* **139**, 891-906 (2009). https://doi.org:10.1016/j.cell.2009.10.027

39 Jones, M. G. *et al.* Nanoscale dysregulation of collagen structure-function disrupts mechano-homeostasis and mediates pulmonary fibrosis. *eLife* **7** (2018). https://doi.org:10.7554/eLife.36354

40 Rubiano, A. *et al.* Viscoelastic properties of human pancreatic tumors and in vitro constructs to mimic mechanical properties. *Acta Biomater* **67**, 331-340 (2018). https://doi.org:10.1016/j.actbio.2017.11.037

41 Sinkus, R. *et al.* Viscoelastic shear properties of in vivo breast lesions measured by MR elastography. *Magnetic resonance imaging* **23**, 159-165 (2005). https://doi.org:10.1016/j.mri.2004.11.060

42 Lee, H. P., Stowers, R. & Chaudhuri, O. Volume expansion and TRPV4 activation regulate stem cell fate in three-dimensional microenvironments. *Nat Commun* **10**, 529 (2019). https://doi.org:10.1038/s41467-019-08465-x

43 Chaudhuri, O. *et al.* Hydrogels with tunable stress relaxation regulate stem cell fate and activity. *Nat Mater* **15**, 326-334 (2016). https://doi.org:10.1038/nmat4489

44 Patel, R. *et al.* Effect of dietary advanced glycation end products on mouse liver. *Plos One* **7**, e35143 (2012). https://doi.org:10.1371/journal.pone.0035143

45 Yan, Z., Yan, H. & Ou, H. Human thyroxine binding globulin (TBG) promoter directs efficient and sustaining transgene expression in liver-specific pattern. *Gene* **506**, 289-294 (2012). https://doi.org:https://doi.org/10.1016/j.gene.2012.07.009

46 Muellenbach, E. A. *et al.* Interactions of the advanced glycation end product inhibitor pyridoxamine and the antioxidant alpha-lipoic acid on insulin resistance in the obese Zucker rat. *Metabolism: clinical and experimental* **57**, 1465-1472 (2008). https://doi.org:10.1016/j.metabol.2008.05.018

47 Zieman, S. J. *et al.* Advanced glycation endproduct crosslink breaker (alagebrium) improves endothelial function in patients with isolated systolic hypertension. *J Hypertens* **25**, 577-583 (2007). https://doi.org:10.1097/HJH.0b013e328013e7dd

48 Ulrich, P. & Zhang, X. Pharmacological reversal of advanced glycation end-product-mediated protein crosslinking. *Diabetologia* **40 Suppl 2**, S157-159 (1997). https://doi.org:10.1007/s001250051437

49 Tao, J. *et al.* Modeling a human hepatocellular carcinoma subset in mice through coexpression of met and point-mutant β-catenin. *Hepatology* **64**, 1587-1605 (2016). https://doi.org:10.1002/hep.28601

50 Zhang, J. *et al.* TEA Domain Transcription Factor 4 Is the Major Mediator of Yes-Associated Protein Oncogenic Activity in Mouse and Human Hepatoblastoma. *Am J Pathol* **189**, 1077-1090 (2019). https://doi.org:10.1016/j.ajpath.2019.01.016

51 Perepelyuk, M. *et al.* Normal and Fibrotic Rat Livers Demonstrate Shear Strain Softening and Compression Stiffening: A Model for Soft Tissue Mechanics. *PloS one* **11**, e0146588 (2016). https://doi.org:10.1371/journal.pone.0146588

52 Bettaieb, A. *et al.* Hepatocyte Nicotinamide Adenine Dinucleotide Phosphate Reduced Oxidase 4 Regulates Stress Signaling, Fibrosis, and Insulin Sensitivity During Development of Steatohepatitis in Mice. *Gastroenterology* **149**, 468-480.e410 (2015). https://doi.org:10.1053/j.gastro.2015.04.009

53 Unno, Y. *et al.* Glycolaldehyde-modified bovine serum albumin downregulates leptin expression in mouse adipocytes via a CD36-mediated pathway. *Annals of the New York Academy of Sciences* **1043**, 696-701 (2005). https://doi.org:10.1196/annals.1333.080

54 Guimaraes, E. L., Empsen, C., Geerts, A. & van Grunsven, L. A. Advanced glycation end products induce production of reactive oxygen species via the activation of NADPH oxidase in murine hepatic stellate cells. *Journal of hepatology* **52**, 389-397 (2010). https://doi.org:10.1016/j.jhep.2009.12.007

55 Fan, W., Li, Y., Kunimoto, K. & Torok, N. J. 3D Imaging of the Liver Extracellular Matrix in a Mouse Model of Non-Alcoholic Steatohepatitis. *J Vis Exp* (2022). https://doi.org:10.3791/63106

Supplementary Files

This is a list of supplementary files associated with this preprint. Click to download.

- SUPPLEMENTARYTablesandtext.pdf